Sulphur solubility of carbonatites as a mass transfer agent in the mantle

Corin Jorgenson

SUBMITTED IN PARTIAL FULFILLMENT OF THE REQUIREMENTS FOR

THE DEGREE OF BACHELOR OF SCIENCES, HONOURS

DEPARTMENT OF EARTH SCIENCES

DALHOUSIE UNIVERSITY, HALIFAX, NOVA SCOTIA

April 2017

Abstract

Carbonatites are rare, mantle-derived igneous rocks with >50 wt% carbon, compared to more typical SiO_2-rich compositions. Whereas the solubility of sulfur for mafic silicate melts has been extensively studied, equivalent data for carbonate-rich compositions has not been obtained. This research will determine the sulfur solubility in molten carbonate to assess the potential for such melts as a mass transfer agent for sulfur, along with precious metals, in the mantle. The goal is to determine the importance of carbonatite metasomatism to establish precious-metal-rich source regions for magmatic ore deposits. The concentration of sulfur at sulfide saturation in molten carbonate was measured as a function of several variables, including melt composition and pressure to assess the sulfur solubility mechanism. Experiments are done using piston cylinder apparatus at the Dalhousie Laboratory for High Pressure Geological Research. Run-products are analyzed using the electron microprobe analyzer using wavelength dispersive spectroscopy and analyzed by laser ablation mass spectroscopy. A synthetic carbonate melt modeled after phase equilibrium experiments with a mantle peridotite assemblage was used. This material is mixed with a similar mass of FeS, doped with 1 wt% each of Ni and Cu, and additional Fe_2O_3, then loaded, along with ~ 5 wt% H_2O, into a graphite-lined Pt capsule. Capsules are placed into a pressure cell comprised of crushable MgO, with an outer graphite furnace, pyrex sleeve, and NaCl sleeve. Run-products consist of a monosulfide solution (MSS) or sulfide liquid coexisting with quenched carbonate melt, represented by a fine-grained intergrowth of carbonate phase and sulfide dendrites. Experiments have been completed up to Fe-oxide saturation by adding up to 30 wt % Fe_2O_3 and the iron content in the carbonate remains quite low, ~4% FeO. The solubility of sulfur in carbonatite melts range from 845-5448 ppm for experiments at 1 GPa, and 107-1502 ppm for the experiments done at 2 GPa. Results suggest slightly higher solubility for carbonate versus silicate melts. The S content shows an exponential dependence on the FeO content of the melt, similar to that of silicate melts and is invariant with temperature and time. The sulfide-carbonatite partitioning of precious metals of Cu and platinum group elements was determined and shows to be similar to the silicate melts, aside from Pt which shows partitioning 2 orders of magnitude higher than the MSS-silicate values. Ru and Ir vary from 2-1 orders of magnitude lower than the MSS-silicate values, and Os has values partitioning one order of magnitude lower than the sulfide-silicate partitioning from the literature. Cu partitioning does not show significant variation with pressure, time, SCSS or iron content.

Keywords: sulfur – solubility – carbonatites – experimental petrology- platinum group elements

Table of Contents

Table of Figures

Table of Tables

Table of Mineral Abbreviations

Mineral	**Abbreviation**
Carbonate	Carb
Clinopyroxene	Cpx
Dolomite	Dol
Monosulfide solid solution	MSS
Olivine	Olv
Orthopyroxene	Opx
Pyrite	Py
Pyrrhotite	Pyh
Sulfide	Sulf

Acknowledgments

Thank you, James for being a wonderful supervisor and teaching me so much about experimental petrology. You have taught me so many new skills which I am very grateful for. Thank you for constantly making time for all my questions, I really appreciate it. This has been such an interesting project and I have learned so much! Thank you.

Thank you to SEG for their generous funding which made the LA-ICP-MS work possible.

Thank you, Bryan, for being my go-to for many questions and having someone to struggle through operating the piston cylinder with.

Thank you to the rest of the lab for their support and help throughout this past year.

Thank you to Dalhousie Earth Science Department for some very happy memories and for teaching me so many valuable skills that have helped me with my honors and that I will take with me as I move forward in my life

Most of all, thank you to my friends and family for their constant love and support.

Chapter 1: Introduction

1.1 Global distribution

Carbonatites are rare igneous rocks with >50 wt% carbon and often found within stable craton settings (Woolley and Bailey, 2012). Carbonatites are often associated with other silica undersaturated igneous rocks such as olivine-poor nephelinites and phonolites (Le Bas, 1987). Ol Doinyo Lengai in Tanzania, which erupted in 2008, is the only active carbonatite volcano. The Fort Portal locality in Uganda is a Quaternary volcanic field which last had volcanic activity 6000-4000 years ago (Baker and Nixon, 1989). Approximately, two-thirds of carbonatites are Phanerozoic and there is common repetition of carbonatite activity during periods of large scale plate movement, which is further discussed below (Woolley and Bailey, 2012).

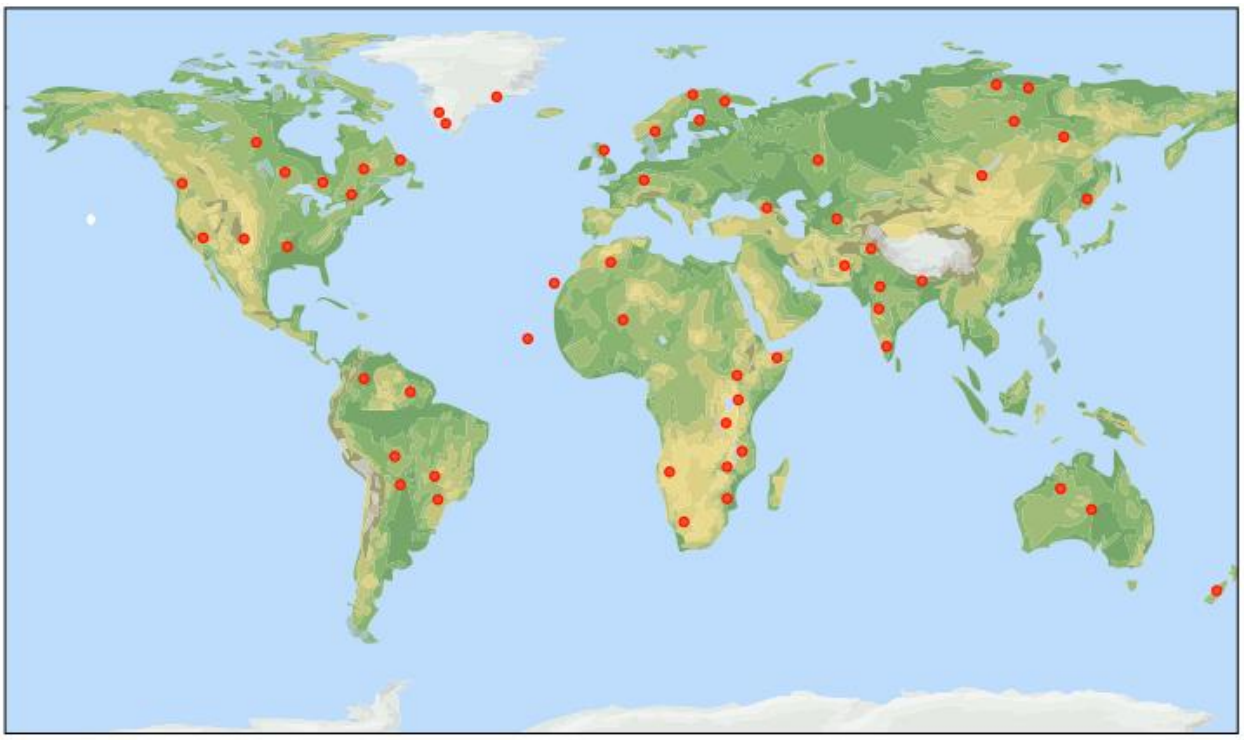

Figure 1.1 Distribution of carbonatites globally. Figure from Jones et al. (2013).

1.2 Geochemistry

Carbonatite melts consist of ionic carbonate, CO_3^{2-} and metal cations such as Ca, Mg, Fe, Na and K (Jones et al., 2013). The geochemical signature of carbonatites includes high abundances of Sr, Ba, P and light rare earth elements (LREE) sometimes over 3 orders of magnitude higher

than chondritic meteorites representative of bulk earth (Nelson et al., 1988). They also show a negative Zr and Hf anomaly relative to similarly incompatible elements (Nelson et al., 1988).

1.3 Petrogenesis

There are multiple theories for the origin of carbonatites including: 1) that they are residual melts from fractionated carbonated nephelinite or melilitite magmas (Gittins 1989; Gittins and Jago 1998), 2) created via immiscibility from a CO_2 saturated silicate melt (Freestone and Hamilton, 1980), and 3) melting of a CO_2 bearing peridotite which generates primary mantle melts (Wallace and Green, 1988). This last possibility is discussed in more detail in section 1.4.

Woolley and Bailey (2012) determined that carbonatites have the same mantle root as kimberlites, since carbonatites tend to occur within the same stable lithospheric terranes and have evidence for mantle metasomatism. The evidence for mantle metasomatism as that many carbonatites have xenoliths or xenocrysts containing assemblages with phlogopite, chrome spinel, chrome diopside, amphibole, and apatite. Woolley and Bailey (2012) postulate that carbonatite magmatism controlled by the lithosphere due to the concentration of carbonatites in the Precambrian area, the repetition of carbonatite activity, doming, and the associated rifting. Carbonatite magmatism is activated when ancient channels in the lithosphere open as a response to plate-wide stress (Woolley and Bailey, 2012).

1.4 Evidence for carbonate melt in the mantle

From the studies of Delpech et al. (2012) and Lorand et al. (2004) there is strong evidence that there is carbonate in the mantle. Both studies analyze mantle xenoliths from the Kerguelen Archipelago which show a high degree of partial melting creating a poikiloblastic harzburgitic mantle stripped of base metal sulfides (BMS) that reacted with carbonate rich silicate melts, re-enriching them in BMS. Delpech et al. (2012) proposed either immiscibility from the silicate-carbonate melt or sulfidation reactions from a CO_2-rich super critical fluid which caused the BMS precipitation. Their study shows evidence via textural and mineralogical features of the BMS for sulfide crystallization from a CO_2 rich vapor exsolved from an evolved carbonate rich metasomatic melt. These include minute sulfide droplets associated with CO_2-rich fluid inclusion trails that cross cut the silicate mineralogy, an assemblage of BMS and dolomite in equilibrium with peridotite matrix, and the absence of micro textural features of liquid-liquid immiscibility. Lorand et al. (2004) focused on the trace elements in the Kerguelen mantle xenoliths. They determined

that from the sympathetic behavior of the Os, Pd, and S that there is transport from a S- and Cl-bearing CO_2 vapor phase in the mantle. CO_2 is similar to sulfur in that is incompatible in a hydrous phase so concentrates in a silicate carbonate melt fraction which in this case was made from an alkaline SiO_2 undersaturated melt (Lorand et al., 2004).

Dolomite and calcite xenoliths in Quaternary basaltic volcanoes in NW Spitsbergen also show evidence for the presence of primary bearing upper mantle carbonate melts (Ionov et al., 1996). The carbonates occur as fine grained aggregates with (Ca,Mg)-rich olivine and (Al,Cr,Ti)-rich clinopyroxene. Ionov et al. (1996) determined that carbonate liquid was formed via decompression melting of the primary carbonates during the transport of xenoliths to the surface.

CO_2 can be brought to the mantle via subduction, this is either recycled and incorporated into the mantle via mineralogical transformations or released to the atmosphere via arc-volcanism (Ammannati et al., 2016). Evidence for carbonate in the mantle can also be seen in kimberlite xenoliths, as seen in the Bultfontein kimberlite in South Africa (Giuliani et al., 2012), the Siddanpalli kimberlite cluster in southern India (Rao et al., 2010), and the Udachnaya-East kimberlite pipe in Siberia (Kamenetsky et al., 2004).

1.5 Phase equilibrium constraints on primary carbonatite formation

The stability of amphibole and carbonate in the mantle controls the stability of the carbonate field as this controls the bulk rock composition and the activity of water (Olafsson and Eggler, 1983; Wallace and Green, 1988). Amphibole is stable to high pressures and temperatures in fertile peridotite (Wallace and Green, 1988). Figure 1.2 shows the stability of carbon-bearing phases as a function of pressure and temperature. At low pressures, CO_2 reacts with peridotite by this reaction:

olv + cpx + CO_2 = dol + opx. (1)

and at higher pressures

dol + opx = magnesite + cpx. (2)

The solidus decreases dramatically at 20 kbar at the point of intersection with the subsolidus low-pressure CO_2 reaction (1). This yields the low pressure bound for carbonate melt formation. Additionally, this phase diagram pertains to small amounts of volatiles, 0.3% H_2O and 0.5-2.5 %

CO_2. With any more of the volatiles a free vapor is stable and any less H_2O will go to the amphibole phase and CO_2 goes to carbonate phase. The enstatite-magnesite-olivine-graphite (EMOG) assemblage buffers these reactions. Olafsson and Egger (1983) also studied the amphibole-carbonate-peridotite phase relationships. They determined the phase relationships between amphibole-spinel-lherzolite assemblages as a function of CO_2/CO_2+H_2O which agrees with phase relations determined by Wallace and Green (1983).

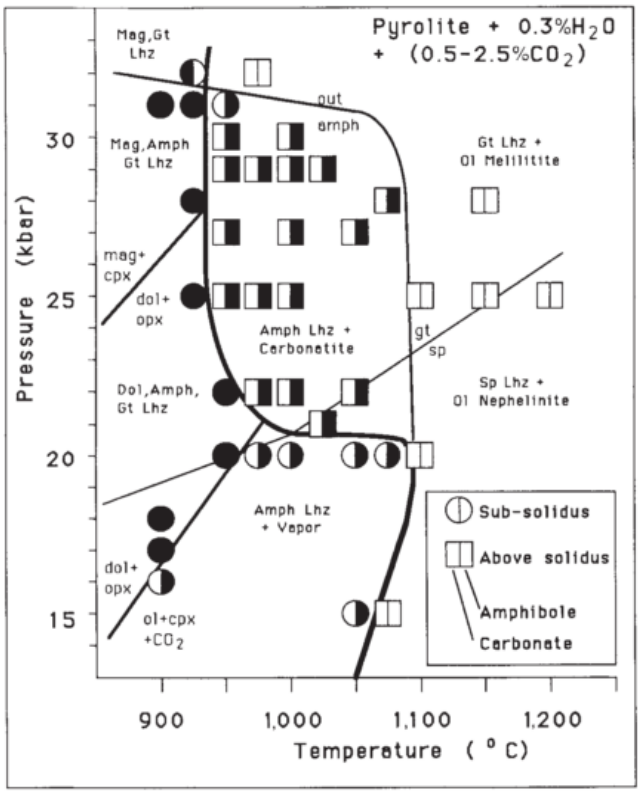

Figure 1.2. Phase relationships for pyrolite (a modal mantle composition) with 0.3% H_2O, and 0.5-2.5% CO_2. These are the amounts below which a vapor phase is not present, with H_2O consumed to form amphibole, and CO_2 to form carbonate. The heavy curve is the solidus, whereas the amphibole-out curve corresponds to the limit of the carbonate melt field. From Wallace and Green (1988).

Figure 1.3 shows the stability limits of mantle carbonate in a calcium free peridotite bulk composition. At low pressure carbonate decomposes to CO_2 vapor. Whereas at more reduced conditions graphite or diamond becomes the stable phase.

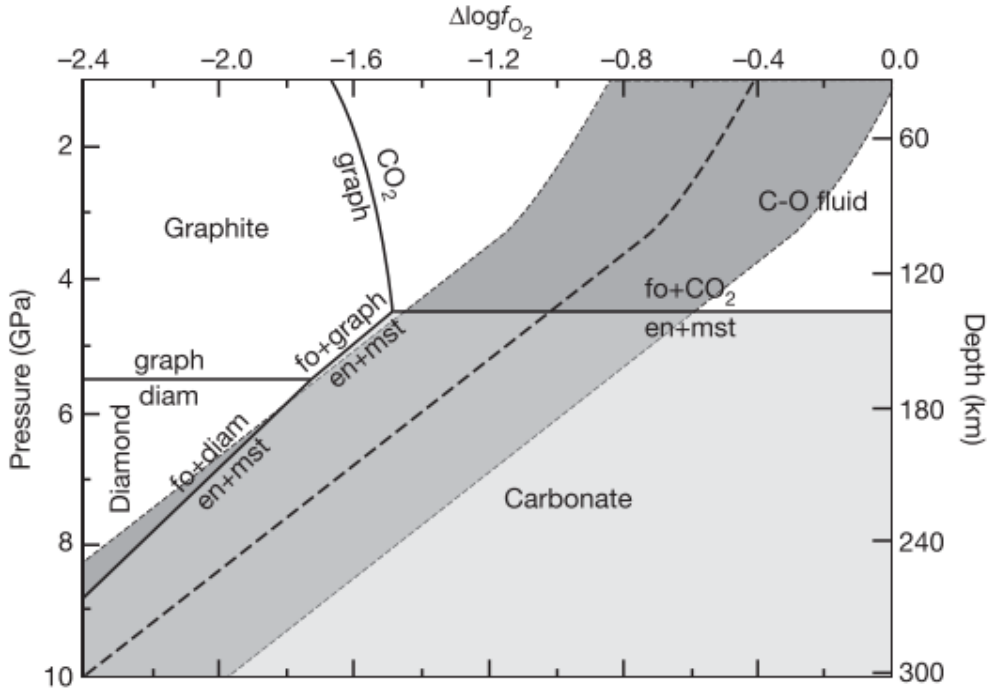

Figure 1.3 The stability limit of carbonate. f_{O2} as a function of depth along an oceanic mantle adiabat. From Dasgupta and Hirschmann (2006)

1.6 Transport properties

Carbonatite melts are extremely mobile. Hammouda and Laporte (2000) used infiltration experiments to demonstrate that such melts can percolate through polycrystalline olivine aggregates very quickly, orders of magnitude larger than basaltic infiltration rates. Cation diffusion in the melt controls the infiltration rate. The infiltration occurs via dissolution/precipitation of olivine grains by the carbonate melt. They propose a migration models in which carbonate melts may travel rapidly in the mantle with the ability to metasomatize regions 10-100 s of meters from their source in 10 ky-1my. This being said, there is a scarcity of carbonatites at the surface which they propose is because small volumes of carbonate melts are difficult to segregate.

Additionally, carbonatites have an extremely low viscosity, as determined by Kono et al. (2014) who did measurements using ultrafast synchrotron X-ray imaging. They determined viscosities to be 0.006-0.010 Pa s, which is 2-3 orders of magnitude lower than basaltic melts at similar conditions. This results in a very high melt mobility; orders of magnitude higher than basaltic melts (Kono et al., 2014).

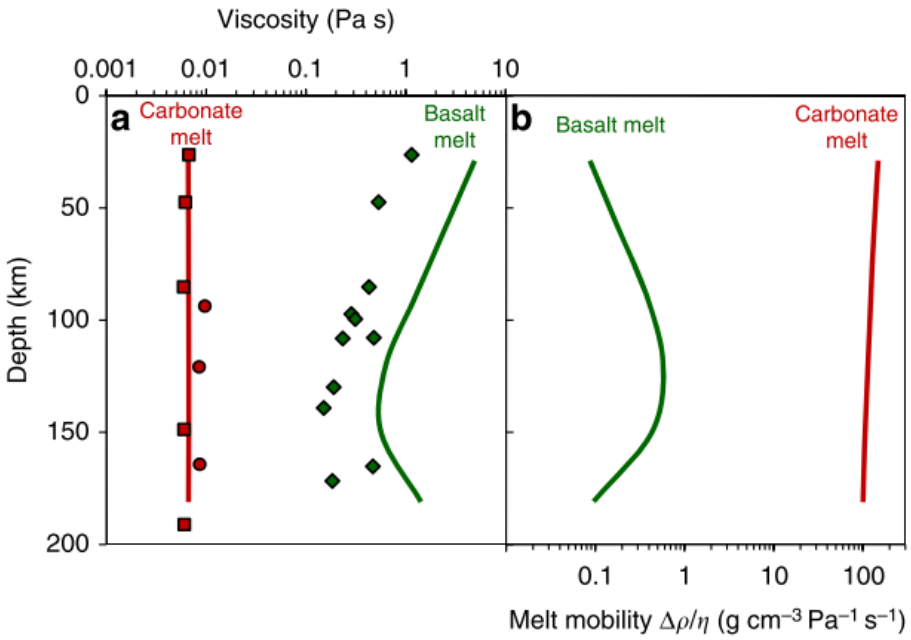

Figure 1.4 Viscosity and melt mobility with respect to depth for a carbonate melt and a basaltic melt. A) At high pressures along the melting temperatures. B) Δρ is the density difference between the solid wall rock and melt, η is the viscosity. (Kono et al., 2014).

Carbonatite melts at low melt fractions remain interconnected up to 0.05 wt% melt in fine grained olivine (Minarik and Watson, 1995). This in turn makes the bulk transport of iron through the polycrystalline solid more efficient than previous estimates, by 2-3 orders of magnitude. Minarik and Watson (1995) determined that the melt remained completely interconnected to 0.05 wt% which corresponds to 0.07 vol% melt for the <63 μm olivine in that study. This indicates that carbonate melts can migrate through the supersolidus mantle at velocities greater than 10 mm/year and at melt fractions of 0.01 vol %, these melts will remain mobile.

Geophysical observations show melting at 300 km beneath ridges which has been determined to be correlated with the solidus of carbonated peridotite (Dasgupta and Hirschmann, 2006). This is much deeper than the solidus of silicate melts. Resulting in an extremely mobile carbonate melt phase at great depths.

Carbonatites are viscous and mobile melts that exist at such depths which has implications for mobilizing incompatible trace elements. Sulfides are associated with carbonatite metasomatism, and it has been suggested that carbonate melt could transfer precious metals in subduction zones (Widom et al., 2003). This indicates that carbonatites could remove sulfides during low degree melting and produce fertile mantle source regions for precious metal rich magmas emplaced in the crust. There are some known cases for high concentrations of platinum group elements (PGE) in

carbonatites. The Loolecop carbonatite deposit in the Phalaborwa Massif, South Africa and the Kovdor Massif in the Kola Peninsula, Russia both have high concentration of PGE, gold, and silver (Rudashevsky et al., 2001). Fontana (2006) also notes five phoscorite-carbonatites pipe complexes that have high concentrations of PGE in Brazil. These examples show the potential for carbonatites to be mass transfer agents for precious metals.

Although it is well known that carbonate melt can effectively transport certain incompatible trace elements, their capacity to mobilize other element groups, such as sulfur and precious metals, is currently uncertain. This could be important as highly mobile S- and metal-rich carbonate melt could account for sulfide-carbonate association seen in some mantle rocks, and could provide a mechanism for generating source regions suitable for crustal mineral deposits. To evaluate this, high pressure experiments were done to measure the solubility of the sulfur in a synthetic carbonate melt. As well, some experiments were doped with PGEs and Re to measure sulfide-carbonate melt partitioning.

The purpose of this experiment is to determine sulphur solubility in carbonatites melts, and how this changes with different parameters will also be investigated. Ultimately, it will be investigated whether carbonatites melts can act as an effective mass transfer agent. Several experiments have been done using a piston cylinder apparatus at Dalhousie University.

Chapter 2: Sulfur Solubility in Magmas

2.1 Sulfur dissolution

Sulfur is an integral element to understand in magmatic systems as it controls the behavior of economically-important elements such as Cu, Ni, Ru, Rh, Pd, Re, Os, Ir, Pt, and Au (Jugo et al, 2005). It is estimated that the mantle has a sulfur content ranging from ~200 ppm (primitive mantle) to ~150 ppm (depleted mantle) (Dasgupta and Hirschmann, 2006).

The sulfur solubility is the sulfur content in a melt saturated with a S-bearing phase. At $f_{O2,}$ more reducing than fayalite-quartz-magnetite equilibrium (FMQ), sulphur atoms can only enter as sulphide in silicate and aluminum melts (Fincham and Richardson, 1954). The sulfur solution is controlled by the relation:

$$\tfrac{1}{2}\, S_2 + O^{2-} = \tfrac{1}{2}\, O_2 + S^{2-} \qquad (3)$$

At oxidizing conditions, in which f_{O2} is greater than 10^{-3}, sulphur exists as sulfate (SO_4^{2-}). In this case, sulfur solution is described by:

$$\tfrac{1}{2}\, S_2 + \tfrac{3}{2}\, O_2 + (O)_{melt} = (SO_4)_{melt} \qquad (4)$$

Here, to ensure that sulphide is the sole sulfur species, experiments conditions in this study will need to be sufficiently reducing. The O^{2-} activity is considered to be constant because the number of O^{2-} anions exceed the number of all other anions including S^{2-} (Mavrogenes and O'Neill, 1999). This in combination with the equilibrium constant for reaction 3 yields the equation for the sulfide capacity (Cs) (Mavrogenes and O'Neill, 1999):

$$Cs=[S/ppm(f_{O2}/f_{S2})^{\frac{1}{2}}] \qquad (5)$$

2.2 Controls on the SCSS

The sulfur content at sulfide saturation (SCSS) is based on the heterogeneous reaction (Mavrogenes and O'Neill, 1999):

$$FeO_{sil} + \tfrac{1}{2}\, S_2 = FeS_{sulf} + \tfrac{1}{2}\, O_2 \qquad (6)$$

The K_{eq} for this reaction, combined with the definition of sulfide capacity from equation 5 and the thermodynamic relationship between the variables in the sulfide capacity gives the following equation for the SCSS (Mavrogenes and O'Neill, 1999):

$$\ln[S/ppm]scss = \frac{A}{T} + B + C\frac{P}{T} + \ln(a_{FeS}^{Sulfide}) \qquad (7)$$

Where A, B, and C are constants dependent on the silicate melt composition, determined experimentally. Although the position of the sulfide saturation surface depends on pressure-temperature and composition, the SCSS of a fixed melt composition is independent of f_{S2} and $f_{O2,}$ aside from their effect on the activity of FeS in the sulfide liquid ($a_{FeS}^{Sulfide}$) (Mavrogenes and O'Neill, 1999).

To validate equation 7, Mavrogenes and O'Neill (1999) performed piston cylinder experiments from 0.5 - 9 GPa and 1400 – 1800 ºC to determine the SCSS in mafic melt compositions. They determined that the SCSS has a strong exponential decrease with increasing pressure as seen in figure 5. They also performed experiments at 1400 ºC, 1500 ºC, and 1800 ºC and found the effect of temperature to be negligible.

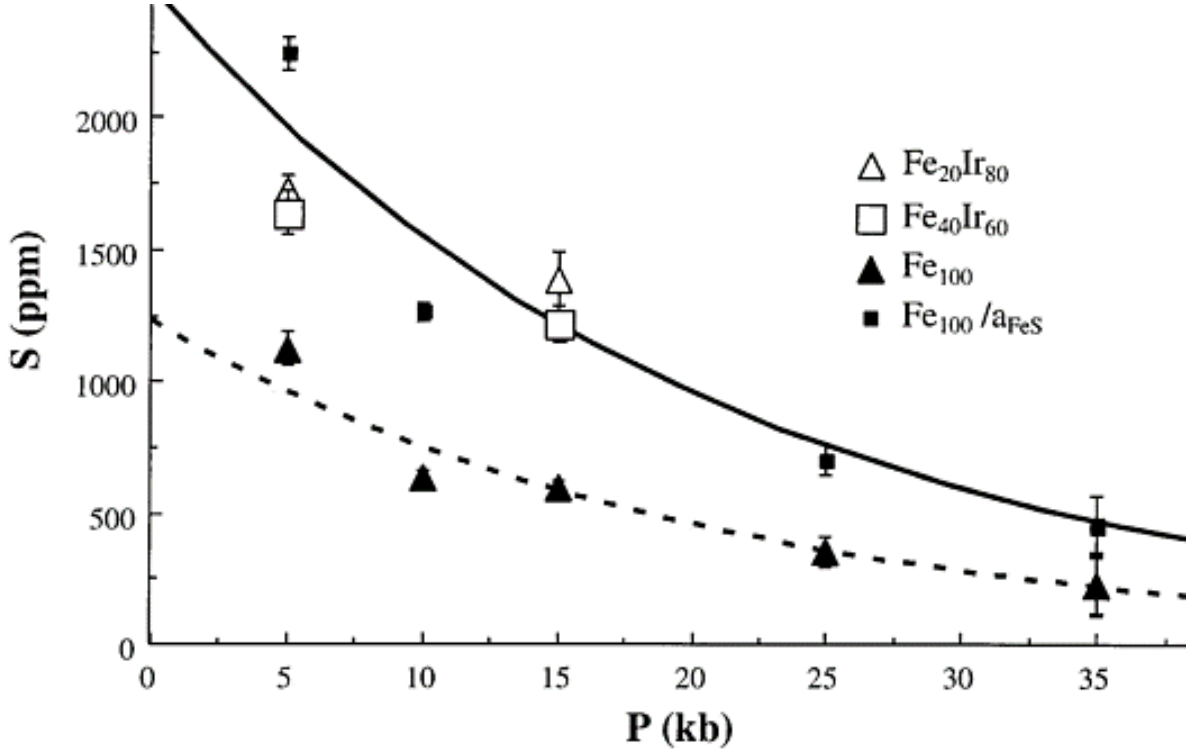

Figure 2.1 Sulfide saturation in synthetic basalt at 1400°C vs. pressure. (Mavrogenes and O'Neill, 1999)

Jugo et al. (2005) measured the solubility and speciation of sulfur in a basaltic system at 1.0 - 1.6 GPa and 1300 - 1355 ºC to document the sulfide to sulfate transition as a function of $f_{O2.}$

They determined that at the silicate melt f_{O2} has a significant impact on sulfur in the basaltic melts, finding an increase of the S content with increasing oxidation. At high f_{O2} the sulfur exists as a sulfate, which they found greatly increases the sulfur content of the melt at saturation. The transition between the sulfide and sulfate occurs at -1 <FMQ <+2. Sulfur contents of the silicate melt at sulfide saturated melt contained (f_{O2} < -1 FMQ) were 0.1- 0.2 wt% S whereas at sulfate saturation (f_{O2}>+2 FMQ) melts contained 1-2 wt% S.

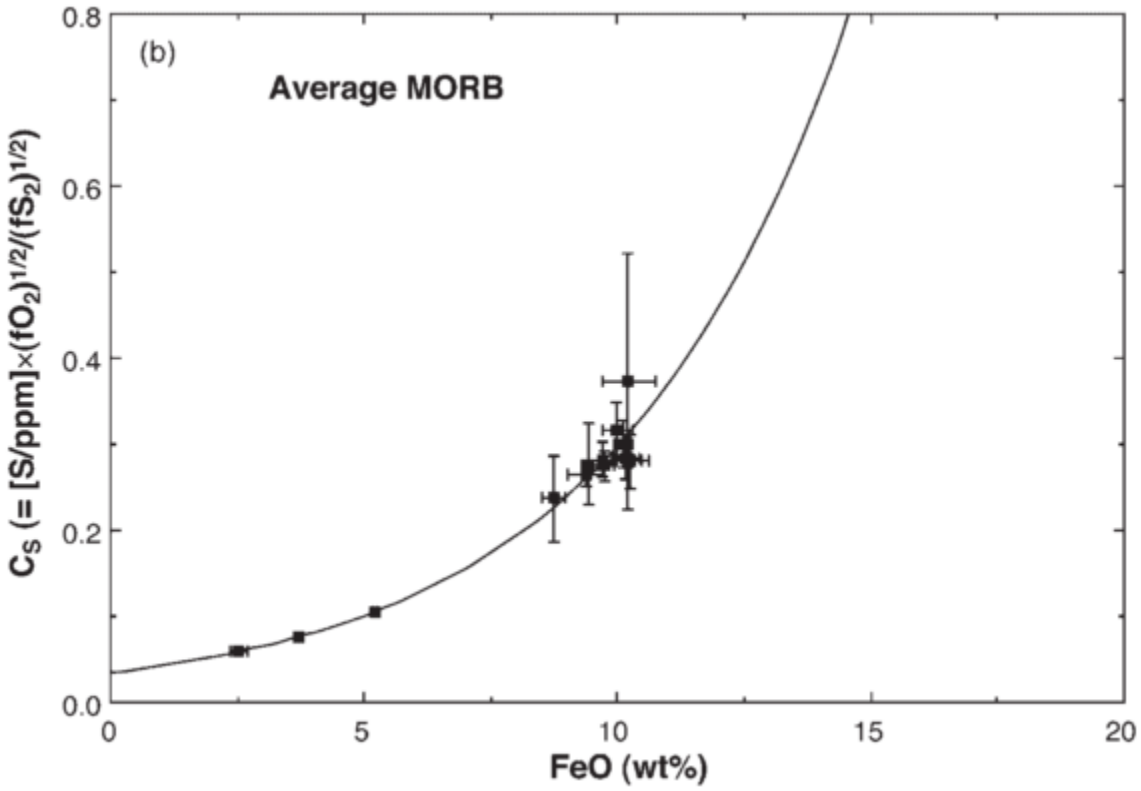

Figure 2.2 Sulfide capacity (Cs) vs FeO wt %, for experiments done at 1400 °C. (O'Neill and Mavrogenes, 2002)

In terms of melt composition effects, FeO content seems to predominate, with both Cs and SCSS exponentially increasing with melt FeO (figure 2.2). O'Neill and Mavrogenes (2002) also note that at low FeO the FeO content does not completely dominate the Cs, but at FeO more than ~10 wt % the other components are irrelevant.

Volatiles can also have a significant effect on the SCSS. Previous studies by Liu et al., (2007) suggested addition of water decreases the SCSS. However, more recent work by Fortin et

al. (2015), determined that water concentration has a positive effect on the SCSS, increasing about 100 ppm per wt% additional H_2O (figure 2.3).

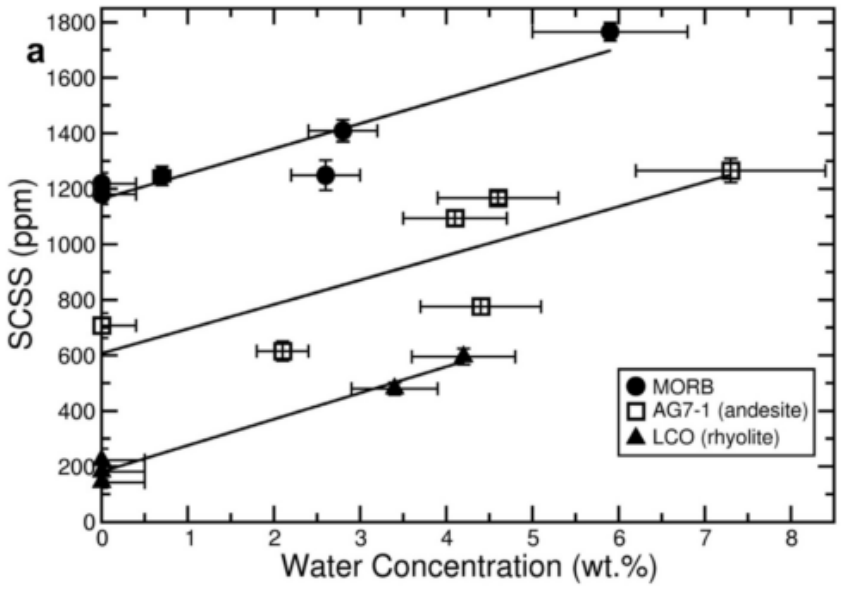

Figure 2.3. SCSS as a function of water concentration (wt%). (Fortin et al., 2015).

2.3 Solubility of sulfur in carbonate melts

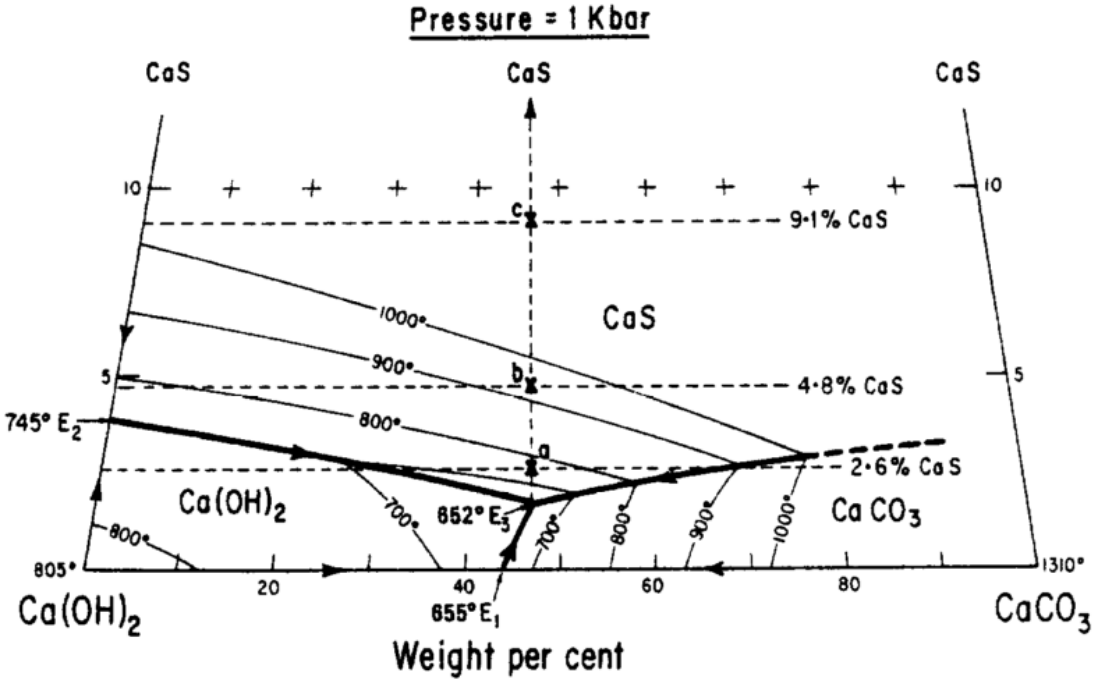

Figure 2.4 Ternary diagram depicting primary phase fields and bounding cotectics for the CaS-$Ca(OH)_2$-$Ca(CO_3)$ system at 1 kbar (Helz and Wyllie, 1979).

In terms of sulfur solubility in carbonate melt, the only previous work is that of Helz and Wyllie (1979), on the CaS-$Ca(OH)_2$-$Ca(CO_3)$ system. They performed experiments at 1 kbar and variable temperatures to determine phase relations which reveal a ternary eutectic at 652ºC. They determined that iron free haplocarbonatitic magmas can dissolve up to 0.9 % sulfide. Their crystallization sequence from the ternary diagram indicates that a melt with little sulfide initially could evolve to nearly 1 % by late stage differentiated. The cotectic in figure 2.4 that separates the $CaCO_3$ and CaS phase fields, corresponds to a CaS content of ~2.6 wt% equivalent to ~11,000ppm sulfur. This is orders of magnitude higher than silicate melts (Liu et al. 2007, Mavrogenes and O'Neill, 1999) and without Fe, which is known to positively effect sulfur solubility (O'Neill and Mavrogenes, 2002). However, measurements were done at low pressure, and previous work (Mavrogenes and O'Neill, 1999) has been shown that SCSS significantly decreases with increasing pressure.

Chapter 3: PGE Partitioning

3.1 Partitioning between silicate melt and sulfides

Mungall and Brenan (2014), measured the PGE partitioning between sulfide melt and silicate melt to determine minimum D^{sulf}_{PGE} values and a model of PGE behavior during melting. Their values are >100 times larger than previous work, due to the different analytical method of using in situ analysis. A summary of the PGE partition coefficients from theirs and previous studies is seen in figure 3.1. The values for the PGEs from the literature range from 10^3 to 10^6, and the values from Mungall and Brenan (2014) range from 10^5 to 10^7.

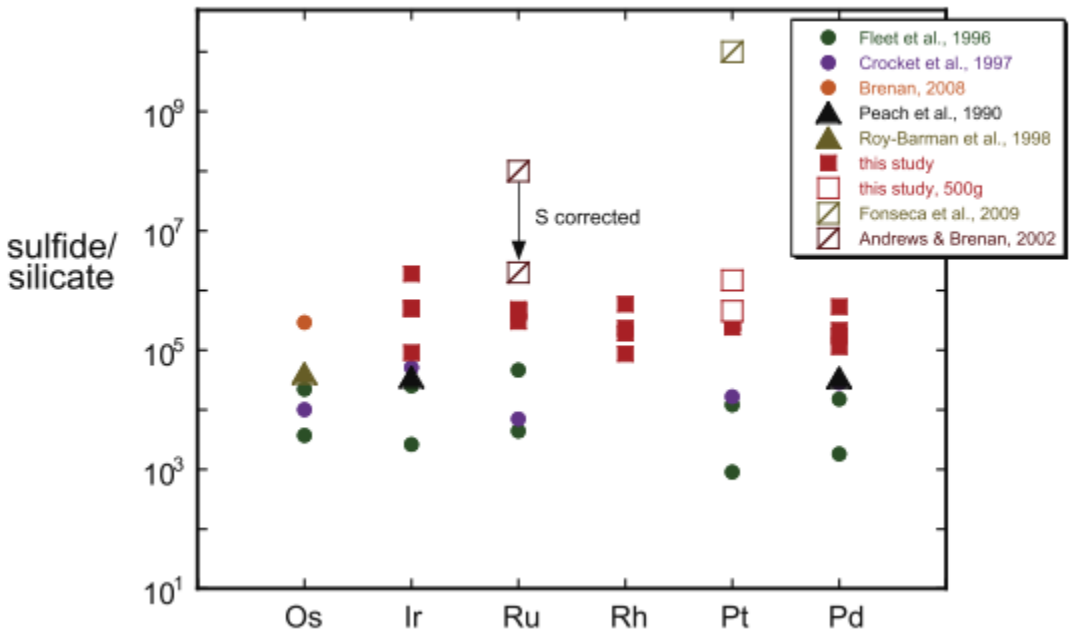

Figure 3.1. Summary of partition coefficients from several measurements involving experimental and natural systems. Values from Fonseca et al. (2009) and Andrews and Brenan (2002) are calculated at FMQ-1, 15 mol% FeO. Using the ratio of pure metal solubility in sulfide and silicate melts. (Mungall and Brenan, 2014).

3.2 Partitioning between silicate melt and carbonatites

Martin et al. (2014) performed silicate melt-carbonate melt partitioning experiments at 1-3 GPa and 1150 – 1260 °C. They determined that under dry conditions the alkali and alkali earth metals partition preferentially into the carbonate melt, whereas the high field strength element (HFSE) go into the silicate melt preferentially, and the REE have partition coefficients around

unity. Under hydrous conditions, values of Cu $D^{carb/silicate}$ ranges from 0.73 to 1.4. For other elements, partitioning under hydrous conditions is very similar, but all the partition coefficients are shifted by up to an order of magnitude, aside for the alkalis. An increase in the bulk silica content had the same effect. They found little effect of f_{O2} or pressure on the partitioning, though pressure has an indirect effect as the solubility of volatiles increases with pressure.

Chapter 4: Experimental and Analytical Methods

4.1 Composition

The carbonatite composition chosen based on an experimental carbonatite melt produced in equilibrium with a peridotite assemblage from Wallace and Green (1988). A mixture comprised $MgCO_3$:$CaCO_3$:Na_2CO_3 in weight proportions 38.95:49.86:11.20 mix. Each oxide was weighed out and ground in a alumina mortar and pestle with ethanol then dried and used. To each sample an additional 5 wt% water was added. The sulfide phase comprised of FeS with 1 wt% each Cu and Ni. Additionally, 0, 15 or 30 wt% Fe_2O_3 was added to vary the FeO content of the melt. Some experiments contain FeS that was doped with an additional 1300 – 4800 ppm Pt, Pd, Rh, Ru, Ir, Os, and Re.

4.2 Control of oxygen fugacity

Graphite capsules were used to control the oxygen fugacity (f_{O2}) by the CO_2-CO-C equilibrium:

$$C_{(graphite)} + O_2 \Leftrightarrow CO_{2\,(fluid)} \quad (8)$$

And

$$C_{(graphite)} + 1/2O_2 \Leftrightarrow CO_{(fluid)} \quad (9)$$

Oxidized carbon species were generated in most experiments by the addition of ferric iron, which is reduced by the reaction:

$$C_{(graphite)} + 3Fe_2O_{3\,(liquid)} \Leftrightarrow CO_{2\,(liquid)} + 6FeO_{(liquid)} \quad (10)$$

Reported oxygen fugacity is based on the calibration of Ulmer and Luth (1991):

$$\text{Log } f_{O2} = \frac{-22324+189P-1.41P^2}{T} + 4.62 \quad (11)$$

For experiments, which did not contain added Fe_2O_3 (SCARB-1 and SCARB-4) the oxygen fugacity is only constrained to be at or below the CCO buffer.

4.3 Piston-cylinder apparatus and sample assembly

The piston cylinder apparatus is a system for generating high pressure on a sample by transferring the load from a hydraulic ram via a tungsten-carbide piston. The sample is contained in a pressure cell (figure 4.1) within a steel die with a tungsten-carbide insert. High temperature is generated by applying power to a graphite furnace which heats the sample. The temperature is

measured with a thermocouple made from W 26% Re and W 5% Re wires. Additionally, water circulated through the upper and lower plates serve to cool the pressure vessel.

Samples are loaded with water and injected with a syringe into graphite lined Pt-capsules then welded shut. Loss of water during welding is mitigated by placing the capsule in a cooled steel holder. The sample is weighed before and after welding and then placed into a drying oven for 30-90 minutes and reweighted to check for water loss. To ensure a minimal temperature gradient the Pt capsule needs to be in the "hot spot" of the graphite furnace, so the crushable MgO is cut and drilled so that the capsule sits in the middle of the furnace. For the ¾" diameter assembly, which the experiments at 1 GPa were done at, the graphite furnace is placed within concentric Pyrex and NaCl sleeves. The NaCl acts to transmit the piston load uniformly and the Pyrex protects the graphite furnace from the salt (figure 4.1). The 3/4" assembly allows for up to three samples to be run at a time. This allows for better reproducibility of pressure and temperature conditions between samples. The ½" assembly, which is used for experiments done at 2 GPa, uses just $BaCO_3$ for pressure transmission. This assembly is then wrapped in Pb-foil and inserted into the pressure vessel. A steel base plug and a pyrophyllite sleeve for the ¾" is inserted on top of this and the thermocouple is inserted into the MgO and the base plug to provide the temperature reading. The ½" assembly used a Pyrex sleeve around the base plug.

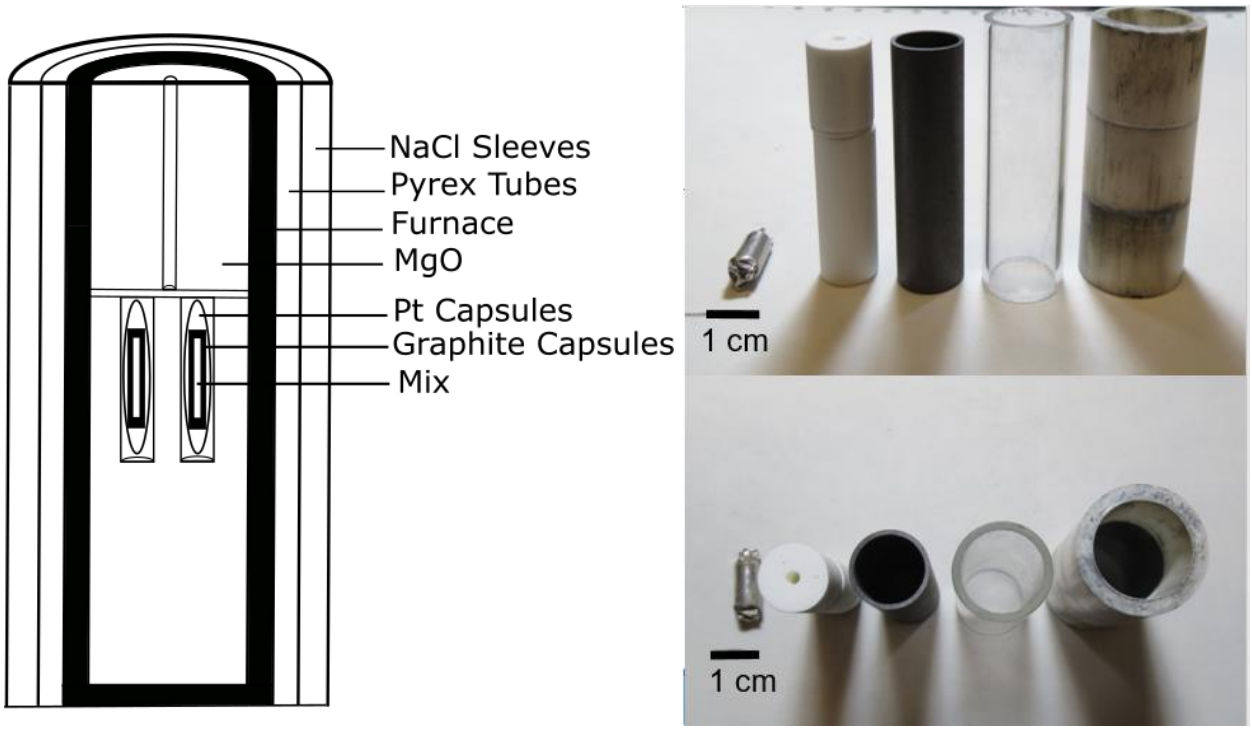

Figure 4.1 Left, cross section of the 3/4" assembly. Right, pictures of the ¾" assembly.

Table 4.1

Summary of experiments

Experiment	P (GPa)	T (°C)	Duration (hr)	Sulfide/Oxide comp [a]	Buffer [b]	Stable phases
SCARB-1	1	1100	48	1:0 $FeS:Fe_2O_3$	<CCO (-10.36)	Carbonate Melt, MSS
SCARB-4	1	1200	24	1:0 $FeS:Fe_2O_3$	<CCO(-9.35)	Carbonate Melt, MSS
SCARB-5	1	1200	24	2:1 $FeS:Fe_2O_3$	CCO(-9.35)	Carbonate Melt, sulfide liquid
SCARB-6	1	1200	24	1:1 $FeS:Fe_2O_3$	CCO(-9.35)	Carbonate Melt, sulfide liquid, Fe-Al spinel
SCARB-8	1	1100	4	1:1 $FeS:Fe_2O_3$	CCO (-10.36)	Carbonate Melt, sulfide liquid, MSS, Fe-Al spinel
SCARB-10	1	1100	12	1:1 $FeS:Fe_2O_3$	CCO (-10.36)	Carbonate Melt, sulfide liquid, MSS, Fe-Al spinel
SCARB-11	1	1100	24	1:1 $FeS:Fe_2O_3$	CCO (-10.36)	Carbonate Melt, sulfide liquid, MSS, Fe-Al spinel
SCARB-14	2	1200	48	2:1 Doped $FeS:Fe_2O_3$	CCO (-8.35)	Carbonate Melt, MSS
SCARB-15	1	1100	48	2:1 Doped $FeS:Fe_2O_3$	CCO (-10.36)	Carbonate Melt, MSS, Pt phase
SCARB-16	1	1100	48	1:1 $FeS:Fe_2O_3$	CCO (-10.36)	Carbonate Melt, MSS, Fe-Al spinel
SCARB-21	2	1200	24	2:1 Doped $FeS:Fe_2O_3$	CCO (-8.35)	Carbonate Melt, MSS

[a] Relative proportion of sulfide to hematite added to experiments

[b] f_{O2} of the CCO buffer from the calibration of Ulmer and Luth (1991) see equation 11 in the text

The experiment is first pressurized to the set pressure, then the temperature is ramped to find the set point at 50 °C/min. The temperature throughout the experiment stays consistent within 1 °C as per the calibrations from the thermocouple. The pressure however drifts and must be adjusted periodically. Nominal pressures are adjusted to account for a 10% friction correction. The system self-quenches at the desired time dropping to the temperature of the circulating water within seconds.

4.4 Sample preparation and electron microprobe analysis

After quenching, the sample was removed from the pressure vessel and the surrounding pressure cell, placed into a 1" diameter mold and back filled with epoxy. Owing to the hydroscopic nature of the quench carbonate melt the samples were prepared in a water-free environment, using baby oil as the polishing medium. Samples were ground with coarse grit (320) to expose the capsule interior, cleaned ultrasonically in acetone then impregnated with epoxy to maintain sample integrity during subsequent grinding and polishing. Finer grits (400 and 600) were then used grind through the impregnation epoxy and expose the full cross section of the sample. 1 µm and 0.3 µm micro alumnia powder were then used to polish the samples, cleaning in acetone after each powder. Samples were then carbon coated for electon microprobe analysis.

Table 4.2 Count times and standards for EMPA analysis.

Element	Count Times: Peak/Background (s)	Standard
Sulfide Analysis		
Fe	20 (10)	Chalocopyrite
Ni	30 (15)	Chalocopyrite
Cu	30 (15)	Chalocopyrite
S	20 (10)	Chalocopyrite
O	20 (10)	Hematite
Carbonate analysis		
Ca	20 (10)	Dolomite
Na	20 (10)	Dolomite
Mg	20 (10)	Dolomite
S	60 (30)	Chalocopyrite
Ni	60 (30)	Chalocopyrite
Cu	60 (30)	Chalocopyrite
Fe	60 (30)	Chalocopyrite

The major element composition of run-product phases was done with a JEOL 8200 Superprobe electron microprobe analyzer (EMPA) housed in the Robert M. MacKay Electron Microprobe Laboratory at Dalhousie University. Samples are bombarded with an electron beam which excites electrons to a higher energy orbitals and x-rays are emitted as the electron settles back to its original energy level. Each x-ray has a characteristic wavelength. Wavelength dispersive spectroscopy (WDS) focuses the x-ray using a diffraction crystals according to Braggs law. Electron dispersive x-ray spectroscopy (EDS) uses a solid-state semiconductor detector to accumulate the full X-ray energy spectrum simultaneously. WDS was used to analyzed for two phases, iron sulfide and carbonate. The count times and standards for the analysis are listed in Table 4.2. The iron sulfide was analyzed fusing a 30 µm focused spot at 50 nA, 15 kV. The carbonate was analyzed using a 30 µm defocused beam at 10 nA, 15 kV.

4.4 Melt reconstruction

The carbonate melt does not quench to a glass, but instead to a heterogeneous intergrowth of quench carbonate phases as well as FeS dendrite making accurate broad beam analysis of sulfur is rather imprecise. To get an accurate analysis of the sulfur content in the melt this effect must be accounted for. The sulfur content in the intergrowth free areas is determined with WDS analysis of the Ca-sulfide in the melt and the sulfur content of the quenched FeS is determined with EDS analysis. Image analysis using Image J software was performed to determine the area of the intergrowths and a mass fraction calculation in equation (12) is done to determine the sulfur content from the intergrowths.

$$S_{TOTden} = \frac{\sqrt{A^3_{sulfide}\rho_{sulfide}}}{\sqrt{A^3_{sulfide}\rho_{sulfide}} + \sqrt{A^3_{carb}\rho_{carb}}} \times S_{den} \quad (12)$$

This is then added to the sulfur content of the carbonate melt to determine the total sulfur, as seen in equation (13). Appendix A lists the full analysis and the error propagation.

$$\sum S_{Total} = S_{matrix} + S_{TOTden} \quad (13)$$

4.5 Laser ablation ICP-MS analysis

Samples were also analyzed for Ni, Cu, and PGE using the LA-ICP-MS facility at the Department of Earth Sciences at the University of Toronto. The system uses a frequency quintupled Nd:YAG laser operating at 213 nm, coupled to a quadrupole mass spectrometer with the ablation cell being flushed by He to enhance sensitivity. The analysis was done at 4-5 Hz laser repetition rate with a 55 μm spot and the stage moving back and forth to generate the analysis. Analysis involved 20 s of background analysis with the ablation cell being flushed with He and 60 s of laser ablation. Each analysis begins with the analyzing the standards twice then analyzing 16 unknowns, then analyzing the standards twice again. The carbonate melt phase in each experiment was analyzed at least 4 times and the sulfide phase from the doped sample was analyzed 3 times. Data reduction was done using the GLITTER version 5.3 software package. A glass standard NIST 610 and JB-sulfide were used as the external reference materials. Ablation yields of the carbonate melt and sulfide were corrected by referencing known concentrations of Ca (melt), Cu (melt), and Ni (sulfide) which were previously determined by electron microprobe analysis. The isotopes measured are ^{43}Ca, ^{60}*Ni*,^{61}*Ni*, ^{63}Cu, ^{65}*Cu*, ^{194}Pt, ^{195}*Pt* for most samples. Some samples were doped with PGEs and for these additional ^{99}*Ru*,^{100}Ru, ^{101}Ru, ^{103}*Ru*, ^{105}Pd, ^{106}Pd, ^{108}*Pd*, ^{185}*Re*, ^{187}Re, ^{189}*Os*, ^{190}Os, ^{191}Ir, and ^{193}*Ir* were analyzed. Multiple isotopes were used to check for interfering iso-bars (elements in italics are the isotopes used for element concentrations). Minimum detection limits (MDL) are at a 99% confidence interval based on Poisson counting statistics, given by:

$$MDL = 2.3 \sqrt{(2B)} \qquad (14)$$

Where B is the total counts in the background interval.

Chapter 5: Results

5.1 Textural development in run-product phases

Sulfides consists of either crystalline MSS or sulfide liquid, as shown in figure 5.1, which is a back scattered electron image (BSE; brightness is proportional to the atomic weight). This shows quenched sulfide liquid which is intergrown with carbonate melt. Average composition for the sulfides is listed in Table 5.1. The sulfide component of the quenched carbonate melt consists of Ca-sulfide and Fe-sulfide, visible as dendrites (figure 5.2). The melt has been analyzed by WDS analysis of the matrix and the melt reconstruction outlined in chapter 3. The major elements of the carbonate matrix and the Ni and Cu content of each experiment can be found in Table 5.2.

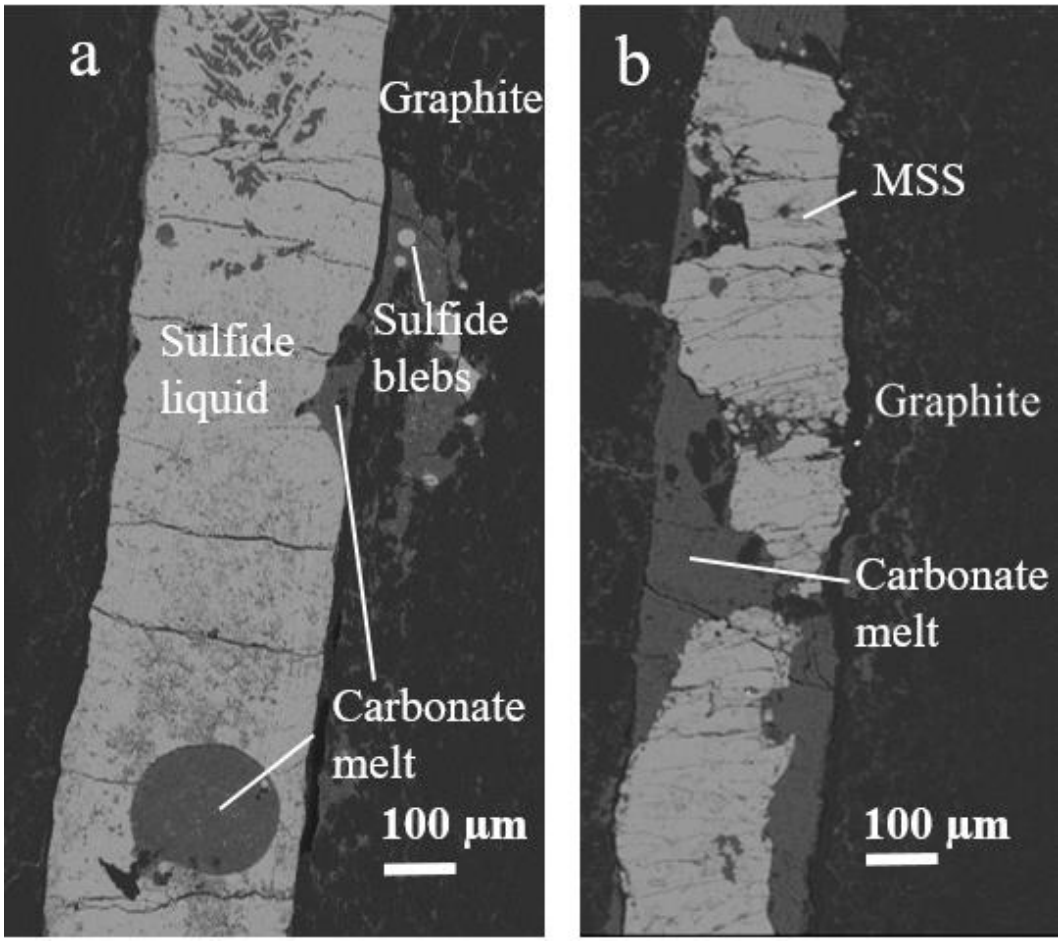

Figure 5.1 Representative back scattered electon (BSE) images of the sulfide portion of run-products. A) SCARB-10, done at 1 GPa and 1100 °C for 12 hours with 30 wt% Fe_2O_3 added, containing quenched sulfide liquid. B) SCARB-16, done at 1 GPa and 1100 °C for 48 hours with 30 wt% Fe_2O_3 added, containing stable MSS.

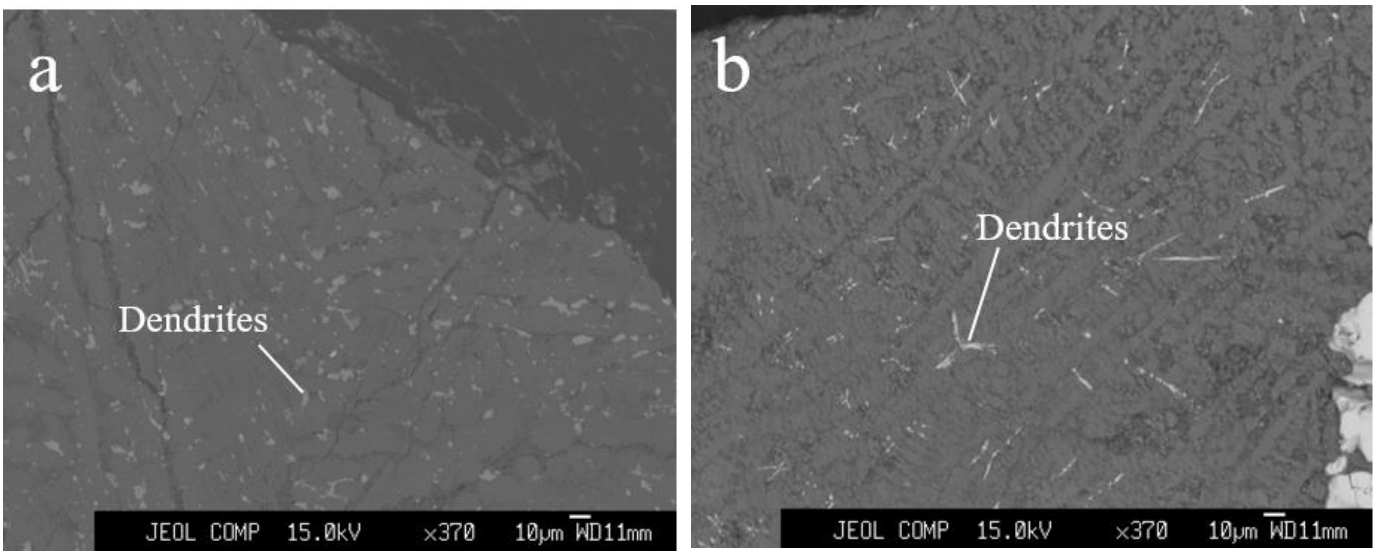

Figure 5.2. BSE images. Representative images of carbonate melt products, both images show quenched sulfide dendrites within the melt. A) SCARB-10, done at 1 GPa and 1100 °C for 12 hours with 30 wt% Fe_2O_3 added. B) SCARB-16, done at 1 GPa and 1100 °C for 48 hours with 15 wt% Fe_2O_3 added.

The intergrowths have an average composition of 57.7 wt% Fe and 29.0 wt % S (Table A2). Majority of the sulfur in the melt is incorporated in these dendrites during the quench whereas additional sulfur is present in other phases (e.g. CaS). To ensure that there was no contamination from the FeS dendrites in the WDS broad beam analysis, the sulfur contents added to the melt reconstruction are from the point analysis with the lowest sulfur. In some cases, the sulfur and the content of the quenched carbonate was below the minimum detection limit, so it is assumed to be negligible. Table 5.2 includes the reconstructed melt compositions; Appendix A has the error propagation and Table A2 has the melt reconstruction data. The FeO content of the carbonate melt presented in Table 5.2 is an average from microprobe analysis. It should be noted the dendrites will also effect the FeO content of the carbonate matrix, but because it is very probable that the point analysis from the microprobe includes these dendrites, the average FeO content from the microprobe analysis is the best representation of the total FeO in the melt.

Table 5.1. Summary of sulfide melt compositions

	wt%			ppm							
	Fe[a]	S[a]	O[a]	Ni[a]	Cu[a]	Ru[c]	Rh[c]	Pd[c]	Re[c]	Os[c]	Ir[c]	Pt[c]
SCARB-1	60.88	37.34	-*	9838	8053	-	-	-	-	-	-	-
err	0.37	0.16		175	297	-	-	-	-	-	-	-
SCARB-4	60.67	38.06	0.84	8422	4663	-	-	-	-	-	-	-
err	0.52	0.45	0.17	234	53	-	-	-	-	-	-	-
SCARB-5	61.97	30.62	5.34	7145	5638	-	-	-	-	-	-	-
err	0.39	0.42	0.37	190	146	-	-	-	-	-	-	-
SCARB-6	61.74	31.22	4.85	7642	4870	-	-	-	-	-	-	-
err	0.42	0.49	0.42	42	65	-	-	-	-	-	-	-
SCARB-8	64.28	23.18	11.90	5985	4565	-	-	-	-	-	-	-
err	0.61	0.69	0.73	61	59	-	-	-	-	-	-	-
SCARB-10	64.63	25.43	10.35	6397	4977	-	-	-	-	-	-	-
err	0.49	1.19	0.86	75	93	-	-	-	-	-	-	-
SCARB-11	62.66	29.62	5.98	5467	3398	-	-	-	-	-	-	-
err	0.37	0.66	0.89	212	295	-	-	-	-	-	-	-
SCARB-14	59.47	37.30	0.84	13021	9226	201	2406	3448	253	410	385	2049
err	0.54	0.67	0.19	419	302	6.5	79	115	9	15	13	73
SCARB-15	60.84	37.86	1.03	10640	9293	<0.43	0.38	0.44	0.30	<0.134	0.91	53.52
err	0.58	0.56	0.26	348	272	-	0.03	0.10	0.01	-	0.17	1.90
SCARB-16	61.93	37.36	0.88	9186	4199	-	-	-	-	-	-	-
err	0.04	0.04	0.01	27	27	-	-	-	-	-	-	-
SCARB-21	59.35	37.26	1.32	12188	6491	484	3534	3795	410	1030	1320	2593
err	0.58	0.30	0.57	393	51	102	73	28	61	124	21	37

Notes: [a] measured with electron microprobe with the exception of Ni and Cu of SCARB 14,15, and 21 which were measured with LA-ICP-MS, [b] is from the reconstructed melt see Table A1, [c] measured with LA-ICP-MS

* O was not measured for SCARB-1, totals valued near 100.

Table 5.2 Summary of carbonate melt compositions

	CaO[a]	Na2O[a]	MgO[a]	CO2[a]	FeO[a]	S [b]	Ni[c]	Cu[c]	Ru[c]	Rh[c]	Pd[c]	Re[c]	Os[c]	Ir[c]	Pt[c]
SCARB-1	29.75	6.97	16.47	46.33	0.70	845	<1.46	<2.10	-	-	-	-	-	-	-
err	0.90	1.29	1.03	0.21	0.10	170	-	-	-	-	-	-	-	-	-
SCARB-4	30.32	6.11	17.93	46.48	0.06	1256	<5.66	15.82	-	-	-	-	-	-	-
err	1.61	1.04	1.17	0.12	0.05	127	-	0.67	-	-	-	-	-	-	-
SCARB-5	29.69	5.00	16.37	46.06	3.30	1568	<3.19	3.46	-	-	-	-	-	-	-
err	1.56	1.70	0.71	0.16	0.56	964	-	3.01	-	-	-	-	-	-	-
SCARB-6	29.30	4.82	16.15	46.33	3.02	1369	<3.62	2.04	-	-	-	-	-	-	-
err	2.67	1.88	1.17	0.27	1.20	859	-	0.43	-	-	-	-	-	-	-
SCARB-8	28.61	4.39	15.83	46.31	4.11	5448	<4.19	4.52	-	-	-	-	-	-	-
err	2.53	2.02	0.93	0.36	1.41	2066	-	1.61	-	-	-	-	-	-	-
SCARB-10	29.19	3.32	15.51	46.41	4.40	3892	<4.48	3.85	-	-	-	-	-	-	-
err	3.11	2.44	0.76	0.28	1.43	2000	-	0.46	-	-	-	-	-	-	-
SCARB-11	28.59	1.70	16.47	46.75	4.92	3229	<3.72	3.33	-	-	-	-	-	-	-
err	3.09	1.38	1.15	0.17	2.21	2048	-	0.86	-	-	-	-	-	-	-
SCARB-14	32.25	1.11	16.05	46.95	2.09	107	<5.01	4.13	<0.05	<0.0045	0.13	0.13	<0.012	0.0005	0.23
err	0.80	0.92	0.59	0.10	0.20	66	-	0.23	-	-	0.01	0.01	0.004	0.0004	0.03
SCARB-15	27.58	4.16	16.37	46.97	3.14	2364	29.46	46.19	<0.04	<0.0021	0.06	<0.013	<0.012	<0.004	0.87
err	2.01	1.24	0.97	0.35	0.79	433	1.91	2.62	-	-	0.01	-	-	-	0.06
SCARB-16	30.54	2.38	17.06	46.98	1.84	568	<3.36	5.00	-	-	-	-	-	-	-
err	2.29	0.95	1.17	0.19	0.35	279	-	3.08	-	-	-	-	-	-	-
SCARB-21	28.43	2.54	19.14	47.62	0.74	1502	<4.78	11.55	<0.03	<0.0022	0.36	0.095	<0.008	<0.003	0.10
err	1.23	1.18	0.77	0.20	0.20	357	-	0.77	-	-	0.03	0.009	-	-	0.01

Notes: [a] measured with electron microprobe, [b] calculated from the reconstructed melt see Table A1, [c] measured with LA-ICP-MS with the exception of SCARB 1, minimum values

In most of experiments where Fe_2O_3 was added, a variety of Fe-Al-Mg spinels were found to be stable (figure 5.3). There were three phases determined using semi-quantitative EDS spot analysis (Table 5.3). There was not any Al additionally added to experiments, suggesting Al contamination from the alumina mortar and pestle that was used to make the carbonatite starting mixture. Wallace and Green (1988) have a small component of Al_2O_3 (1.95 wt %) in their carbonatite that co-existed with a peridotite assemblage so this does not pose a serious problem. In most experiments the amount of Al in the melt is <1 wt%.

Table 5.3 Spinel Phase compositions

	SCARB-11/ -16	SCARB -10	SCARB-8
Mg	19.32	5.43	9.93
Al	57.77	10.32	11.66
Fe	22.78	84.26	58.52
Ca	-	-	10.35
Na	-	-	4.00

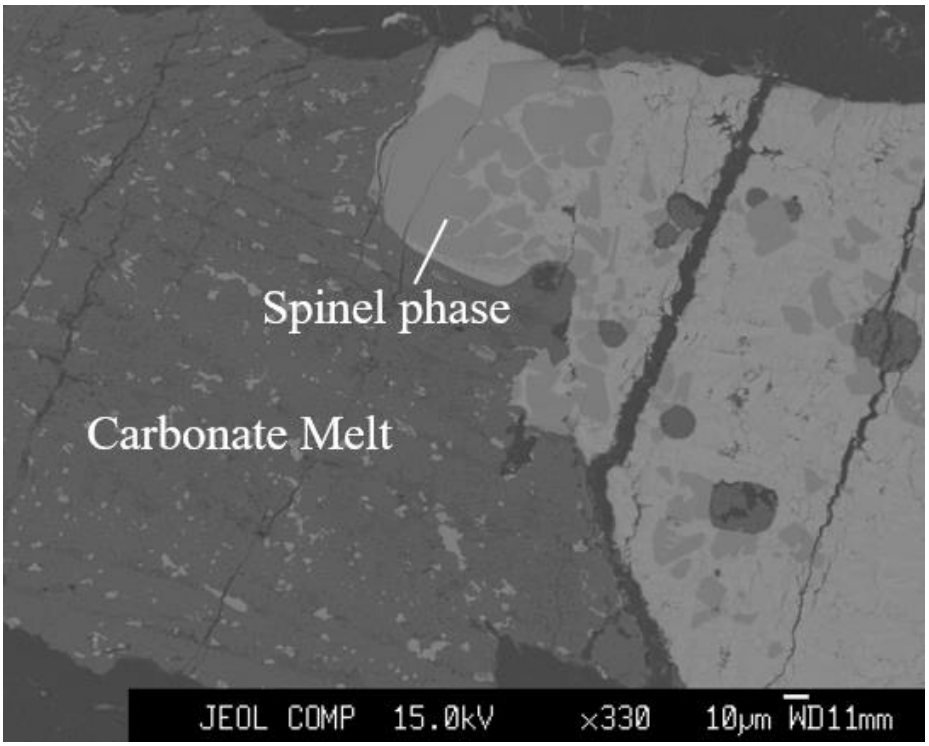

Figure 5.3 BSE image of SCARB-10 showing representative images of the spinel phase. Run conditions of 1 GPa and 1100 °C for 12 hours with 30 wt% Fe_2O_3 added.

5.2 Analytical results

Figure 5.4 shows the SCSS (ppm) as a function of the FeO content of the carbonate melt for experiments at 1200 °C and 1100 °C. The plot shows a trend of exponential increase of S

content with increasing FeO. A linear trend could potentially fit as well, but an exponential function seems more probable given the function for silicate melts. The trend is prominent for the experiments at 1100 ºC and the data from the experiments at 1200 ºC shows a projected trend with the same dependence. This suggests a negligible temperature dependence. At FeO between 0-3 wt% the sulfur in the melt ranges from 500 – 2500 ppm, and at 3-5 FeO wt% there is an increase with the S content ranging from 3000 – 5500 ppm.

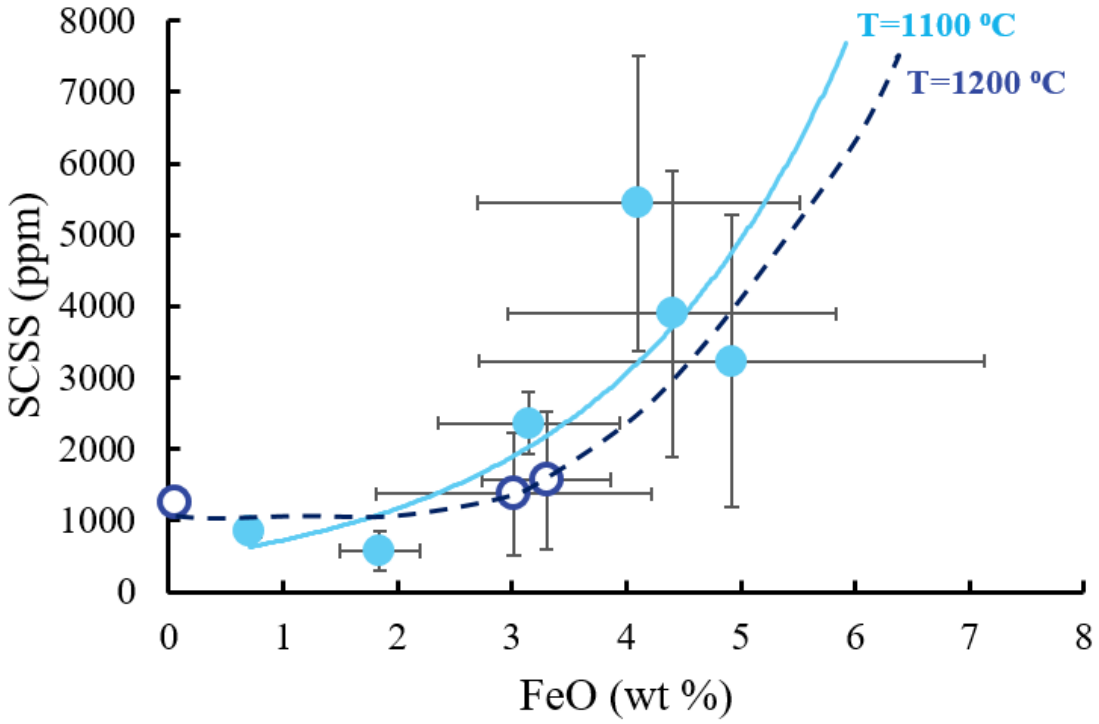

Figure 5.4 SCSS as a function of FeO wt% in the carbonate melt. T=1100ºC and T=1200ºC are both done at 1 GPa and Fe_2O_3 wt% added varies.

Figure 5.5 shows the FeO wt% as a function of Fe_2O_3 wt% added. This is a representation of how insoluble FeO is in the carbonate melt at the conditions of the experiments. Despite adding 15 or 30 wt% Fe_2O_3 to the experiments the FeO content of the melts does not contribute more than 5 wt% FeO to the melt, with the remainder forming Fe-bearing spinel.

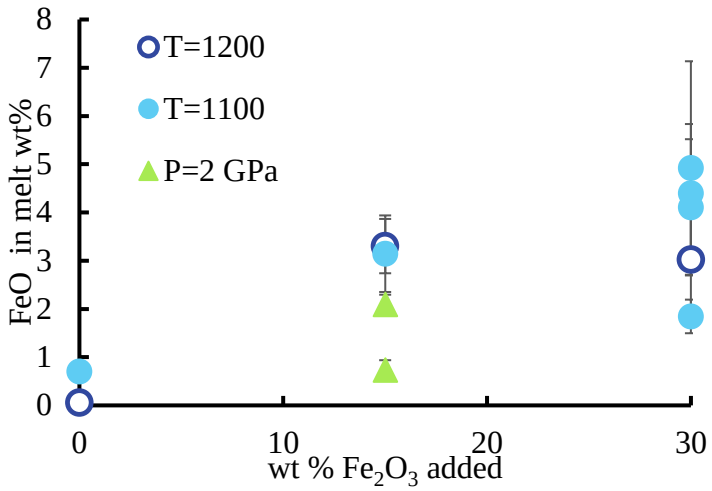

Figure 5.5. Wt% FeO added with respect to wt% FeO in carbonate melt. This is a representation of how insoluble FeO is in the carbonate melt at the conditions of the experiments. Experiments at 1100°C and 1200°C are both done at 1GPa. The experiments at 2 GPa are done at 1200 °C

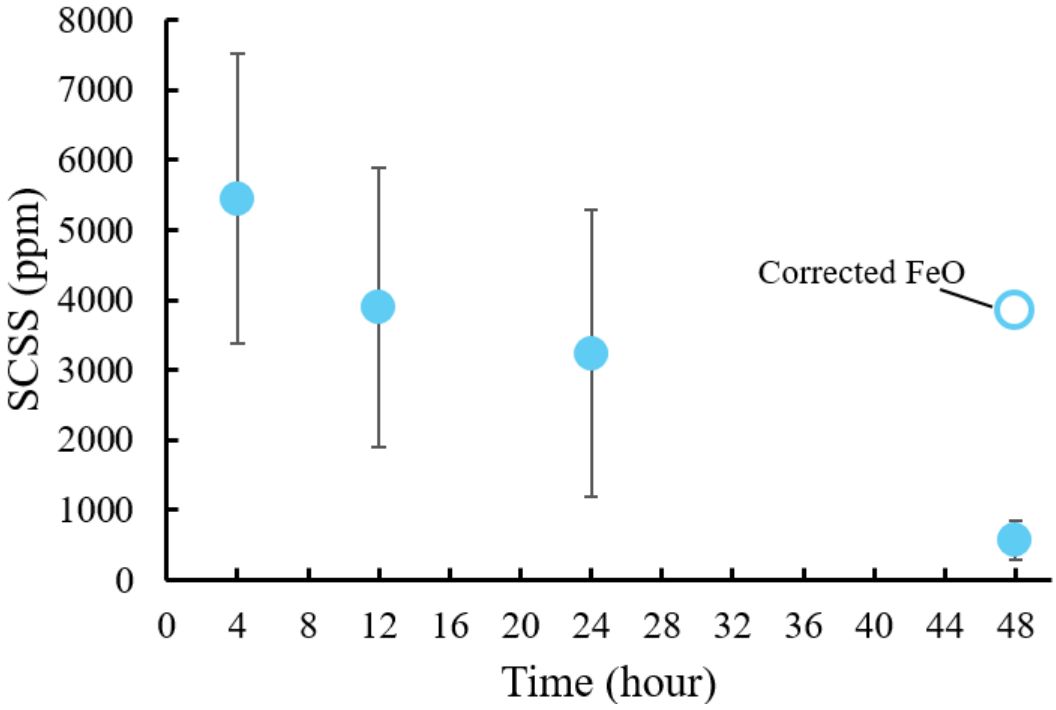

Figure 5.6. SCSS as a function of time, at 1 GPa and 1100 °C. All samples had an additional 30 wt% Fe_2O_3 added. Point at 48 hr is corrected, as described in text.

The data in figure 5.6 shows that the S content ranges from 3000 to 6000 ppm, and all data is within error consistent with experiments reaching equilibrium. Although, this excludes that data point at 48 hours which shows a much lower S content of 568 ppm. However, this sample has an anomalous low FeO content, 1.8 wt %, as opposed to the other which have FeO wt% of 4.1, 4.4, and 4.9 for SCARB-8,-10, and -11 respectively. If the sulfur content is corrected to the same FeO

content (4.5 wt%) of the other experiments in the time series (figure 5.4), 3800 ppm, then values agree for the entire time interval investigated.

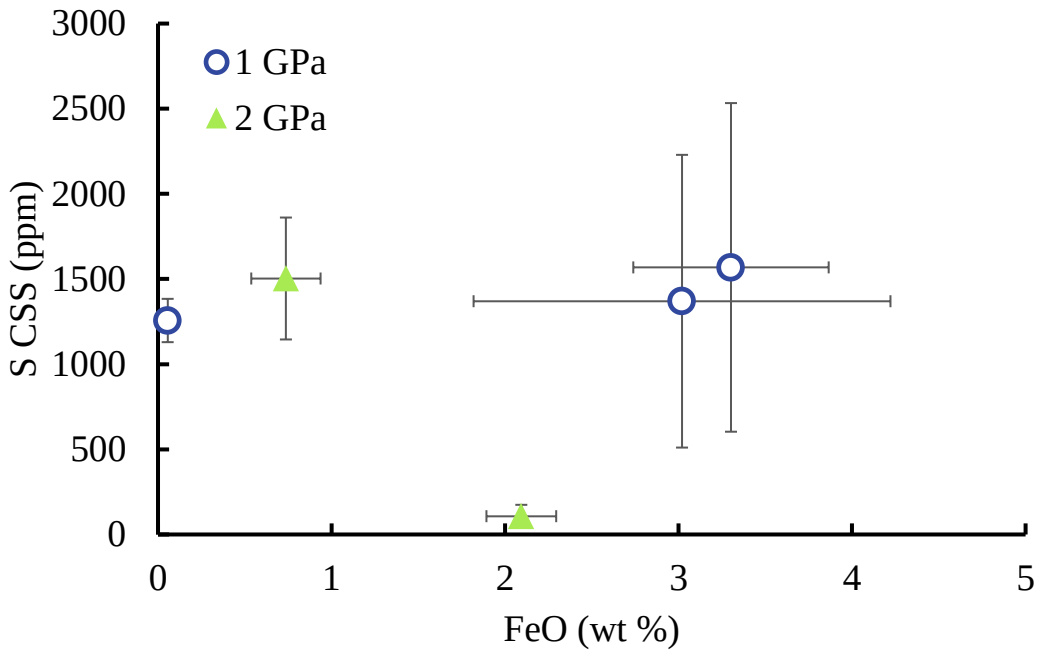

Figure 5.7 Sulfur solubility as a function of FeO wt% for experiments done at 1 and 2 GPa, 1200 ºC, and varying duration.

Figure 5.7 shows data from the experiments done at 1 and 2 GPa, indicating a null or negative effect of pressure on the sulfur solubility. SCARB-14 shows a much lower solubility of 107 ppm where SCARB-21 shows a S content of 1503 ppm which is quite similar to the 1 GPa values. As only 2 experiments were done at 2 GPa, further research would be required to determine a conclusive relationship.

5.3 LA-ICP-MS analysis

Figure 5.8 shows a reflected light image of a representative sample, SCARB-11, before and after laser ablation. Each sample was doped with 1 wt% each of Ni and Cu, and some samples with additional PGE. A summary of the Ni, Cu, and PGE contents in the samples is provided in Table 5.1 and 5.2.

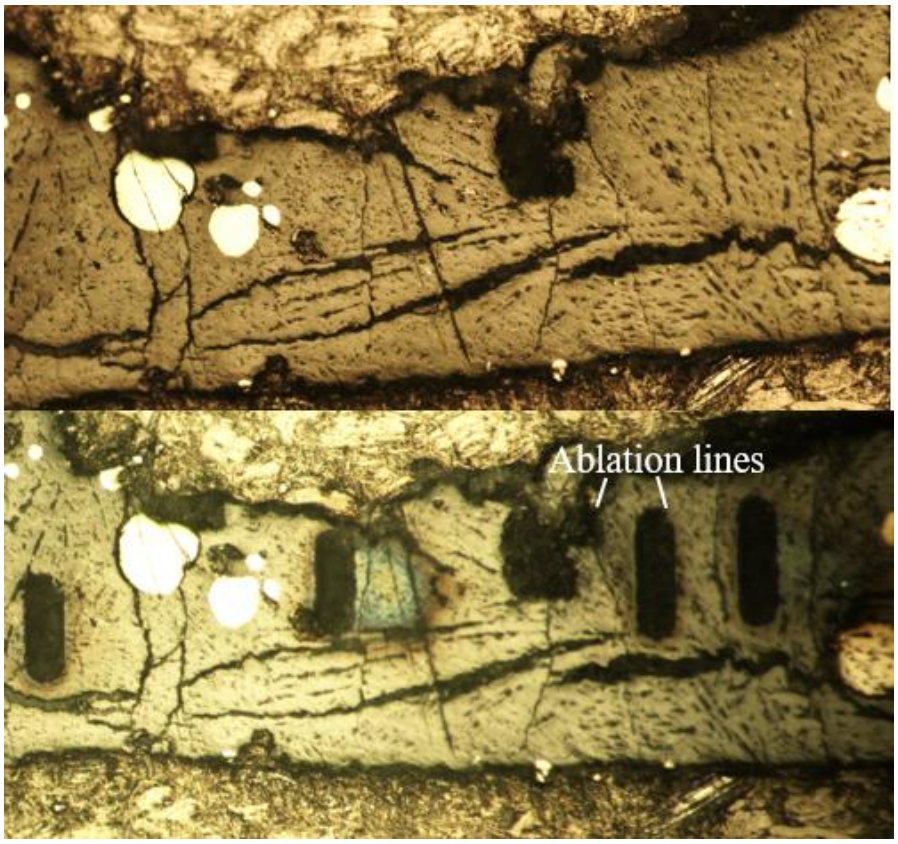

Figure 5.8 Reflected light images of SCARB-11 before (top) and after (bottom) laser ablation. 55µm lines.

The time resolved spectra for Cu (figure 5.9) relative to Ca show a homogenous distribution throughout the ablation. The Cu content in the melts (Table 4) range from 2.0-5.0 ppm apart from SCARB-4 (15.82 ppm), SCARB-15 (46.2 ppm), and SCARB-21 (11.55 ppm). Partition coefficients are presented in Table 5.4 and range from 201 to 2233. It should be noted that all samples had the Cu and Ni content in the melt analyzed with the LA-ICP-MS but only SCARB-14, -15, and -21 had the sulfides measured as well. For all other samples the Cu in the sulfide content is measured with the microprobe. SCARB-4, -15, and -21 have partition coefficients much smaller than the other samples, this difference does not seem to be systematic and does not have a dependence of FeO, SCSS, pressure, time or temperature. It is possible that the variation arises from changes in the oxygen fugacity which is not measured directly in these experiments. Also noted are the difference in the sulfide phase present. SCARB-4, -14, -15, -16, and -21 all have the MSS phase, where SCARB-5 and -6 have sulfide liquid and SCARB-8, -10, -11 have both phases stable. There does not appear to be a systematic difference in the partitioning between these

difference phases. The data collected for Ni in the carbonate melt is below the detection levels, so is not presented here.

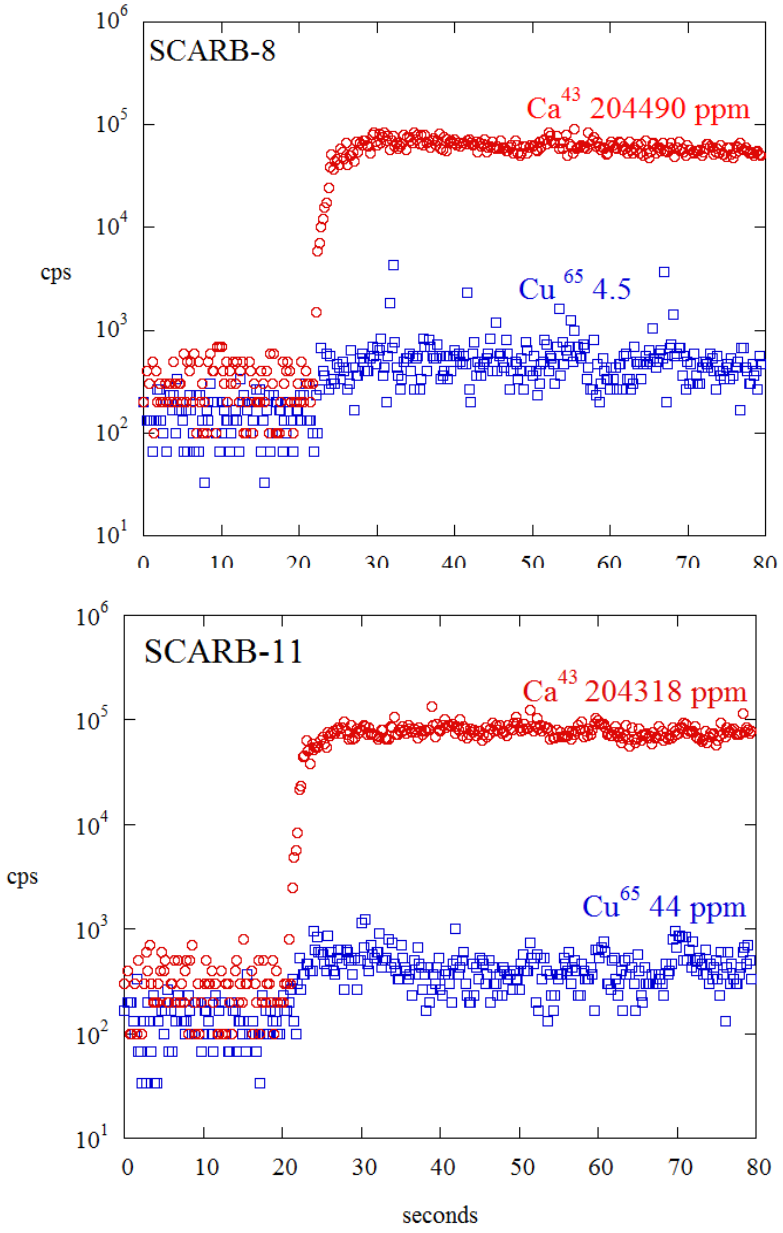

Figure 5.9 Time resolved spectra for LA-ICPMS analysis of carbonate melt. SCARB-8 done at 1 GPa, 1100 ºC, 4 hours with 30 wt% Fe_2O_3 added. SCARB-11 done at 1 GPa,1100 ºC, 24 hours with 30 wt% Fe_2O_3 added. Signals for Cu show a homogeneous signal compared to Ca.

Table 5.4 Sulfide-Carbonate melt Cu partition coefficients

	$D^{sulf/carb, Cu}$
SCARB-4	295
SCARB-5	1631
SCARB-6	2384
SCARB-8	1009
SCARB-10	1293
SCARB-11	1021
SCARB-14	2234
SCARB-15	201
SCARB-16	840
SCARB-21	562

Table 5.5. Summary of sulfide/carbonate melt PGE partition coefficients

	Ru	Rh	Pd	Re	Os	Ir	Pt
SCARB-14	4.11×10^{3}	5.35×10^{5}	2.63×10^{4}	1.88×10^{3}	4.23×10^{4}	7.55×10^{5}	9.03×10^{3}
SCARB-15	1.10×10^{1}	1.82×10^{2}	6.88	2.42×10^{1}	8.09×10^{-1}	2.26×10^{2}	6.13×10^{1}
SCARB-21	1.61×10^{4}	1.61×10^{6}	1.07×10^{4}	4.31×10^{3}	1.29×10^{5}	5.28×10^{5}	2.65×10^{4}

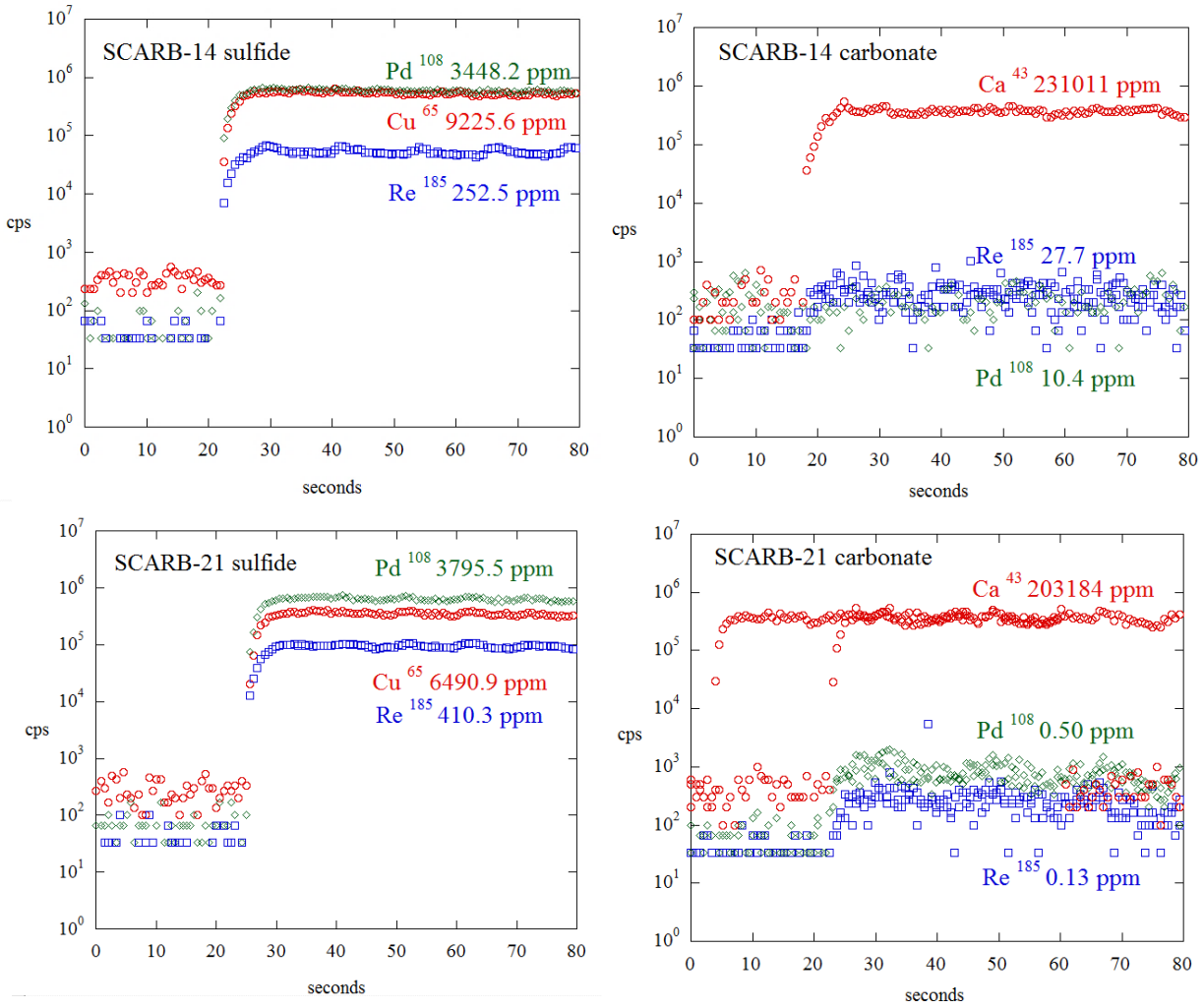

Figure 5.10 Time resolve spectra for LA-ICPMS analysis for carbonate melt (left) and the sulfide (right). SCARB-14 done at 2 GPa and 1200 °C for 48 hours with 15 wt% Fe_2O_3 added, SCARB-21 done at 2 GPa and 1200 °C for 48 hours with 15 wt% Fe_2O_3 added. Signals for both Re and Pd show homogenous signals relative to the Ca and Cu, suggesting constant distribution of PGEs in the sulfide and carbonate melt.

The signals for Pd and Re in the carbonate melt and sulfide show homogenous signals relative to Ca and Cu indicating that these PGE are distributed homogeneously in these samples (Figure 5.10). Not all spectra showed this homogeneity, some showed peaks and troughs indicating a non-homogenous melt. The concentrations of the PGE can be found in Table 5.1 and 5.2. Values for the PGE partition coefficients can be found in Table 5.5 and the calculations to determine the coefficients can be found in Appendix B. The values for the PGE in the sulfides is much higher than that of the carbonate melt, indicating preferential partitioning into the sulfide phase.

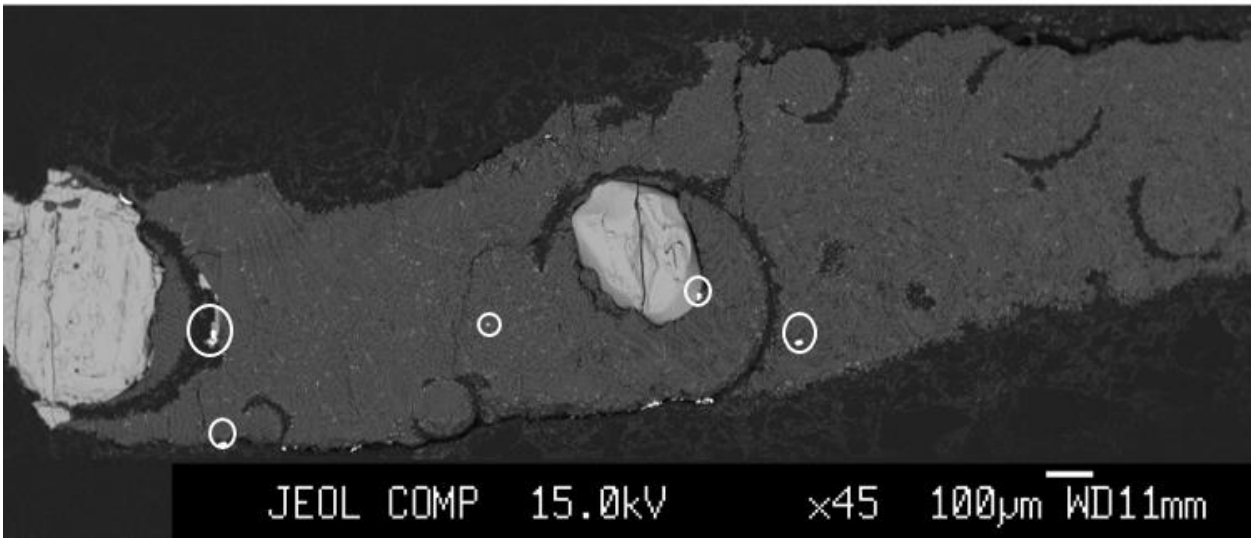

Figure 5.11 SCARB-15, 1GPa, 1100 °C, 15 wt % Fe2O3 added, and doped. White circles show Pt rich phases.

Table 5.6 Composition of the Pt phase

	wt %
Pt	95.70
Ru	0.11
Rh	0.14
Pd	0.19
Os	0.34
Ir	1.12
S	0.17
Ca	0.70
Fe	1.23
Mo	0.14

A quick note on SCARB-15 must be made, SCARB-15 was initially doped but it seems the PGEs partitioned into large Pt-blebs (figure 5.11). The composition of these blebs is noted in Table 5.6. This is anomalous and the only doped sample that conditions (1GPa and 1100 °C) so there is not enough data to provide any realistic conclusions. AS there is significant uncertainty with this sample it will not be included in the discussion on PGEs.

Chapter 6: Discussion

6.1 Sulfur solubility

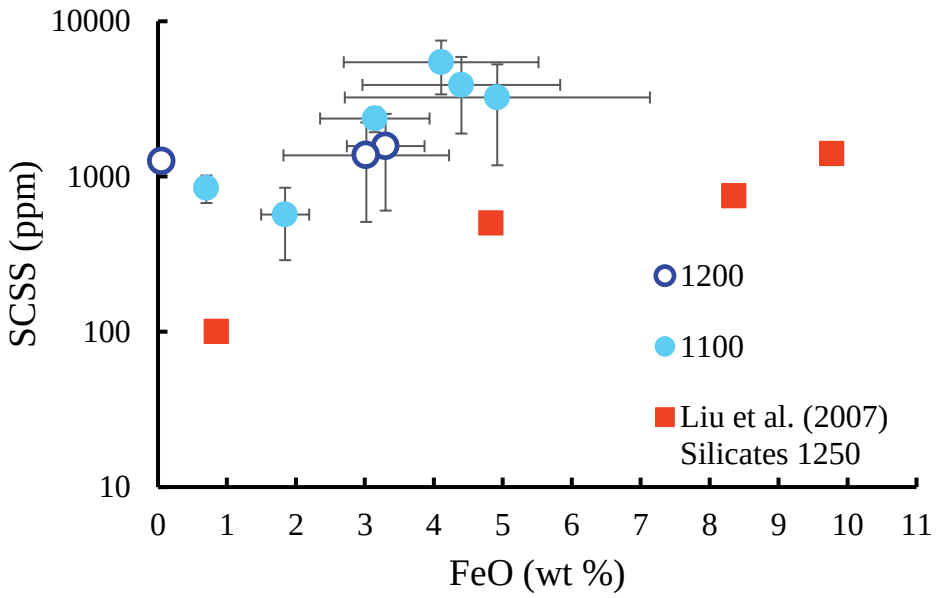

Figure 6.1 Sulfur solubility as a function of FeO in silicate and carbonate melts. Experiments at 1100 °C and 1200 °C for this study are compared to data from Liu et al. (2007) for experiments done at 1250 °C on silicate melt. All experiments at 1 GPa.

The solubility of sulfur in the carbonate melt is nearly an order of magnitude higher than silicate melt, as seen in figure 6.1. When compared to data from O'Neill and Mavrogenes (2002) the sulfur content at similar FeO content also shows a similar variation by an order of magnitude. This indicates that carbonate melt have a greater capacity to transport S in the mantle than silicate melts. Additionally, the exponential trend between the FeO wt% and the sulfur in silicate melts (O'Neill and Mavrogenes, 2002, and Liu et al., 2007) is seen in carbonate melts as well.

Two experiments at 2 GPa were completed, for which an initial estimate of the pressure effect can be determined (figure 6.2). Mavrogenes and O'Neill (2000) showed that an increase in pressure reduces the SCSS. This data suggests a negative or null dependency on pressure. However, a more thorough pressure series should be completed to get a better sense of the nature of the dependency.

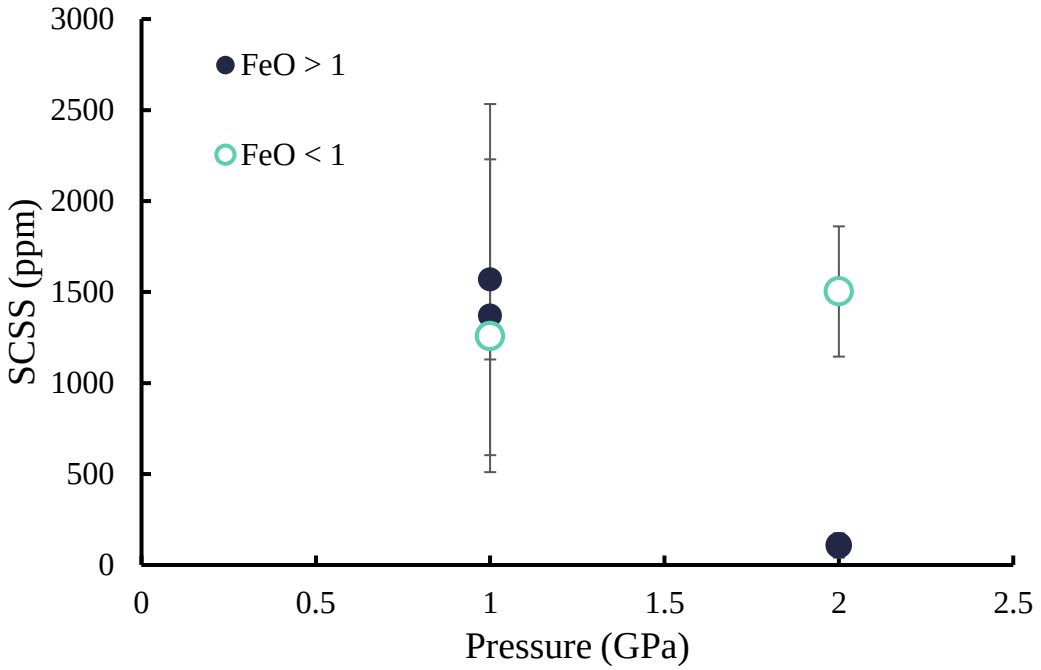

Figure 6.2. Sulfur as a function of pressure for experiments done at 1200 °C. FeO content changes the sulfur solubility as previously discussed so the FeO content is stated

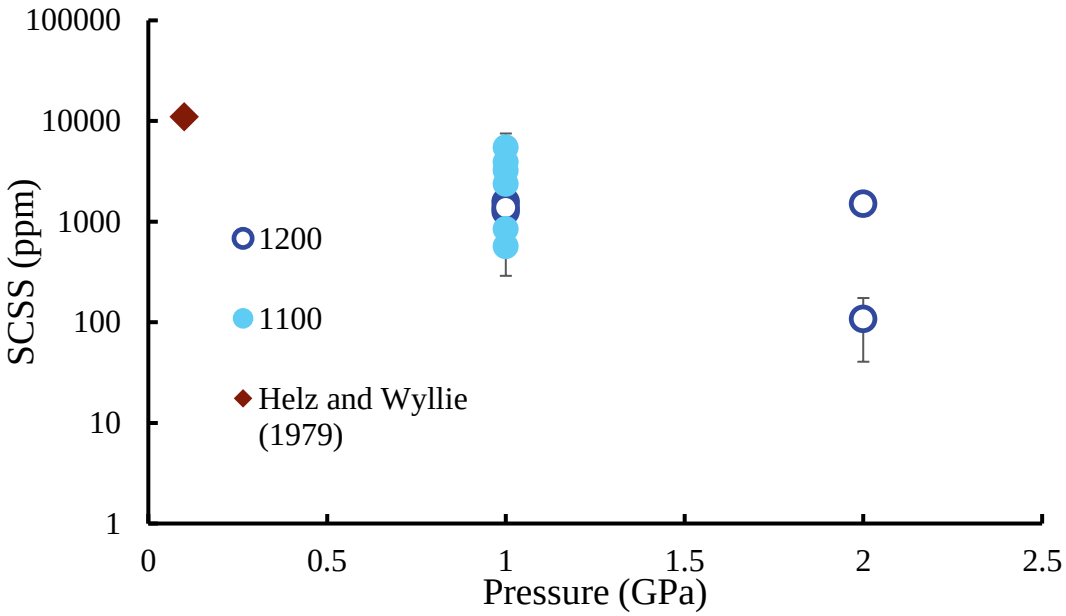

Figure 6.3 Sulfur solubility as a function of pressure. Helz and Wyllie (1979) data is at 655 °C and Fe free. Data from this study ranges in wt% FeO

When compared to the Helz and Wyllie (1979) data (figure 6.3), sulfur solubility measured in this study is 10x lower, which could be a result of the lower pressure of their experiments. Although there is not a conclusive pressure dependency it is expected that at lower pressures the sulfur solubility will increase as it does in silicate melts, which may explain why Helz and Wyllie data is so much higher than that found in this study.

6.2 Cu and PGE partitioning

The Cu sulfide carbonate melt partition coefficients range from 10^2 to 10^3. This is somewhat lower than the $D^{sulf/silicate}$ from Mungall and Brenan (2014), determined the partitioning between sulfide liquid and silicate melt to be ~10^3. This indicates that carbonate melts have a similar ability to transport Cu in the melt to silicate melts. It is important to note here that the f_{O2} between these two studies is quite different Mungall and Brenan (2014) have their experiments from ΔFMQ -1.1 to -1.3 where the experiments of this study were done at CCO -8.35 to -10.36 which corresponds ΔFMQ of -0.7 to 0.1 which is more oxidizing. Additionally, their experiments were also done at ambient pressure whereas for this study they were done at 1-2 GPa. $D^{MSS/sulfide\ melt}$ values for Cu were determined by Mungall et al. (2004) to be ~10^2. This is within the range of this data, indicating there is also a similar Cu partitioning for carbonate melt and silicate melt between the MSS but Cu is slightly more compatible in silicate melts.

Partitioning of the PGE in SCARB-14 and -21 are consistent with each other varying no more than an order of magnitude (figure 6.4). Both SCARB-14 and -21 have the sulfide stable as MSS. $D^{MSS/silicate}$ values in figure 6.4 are calculated from multiplying known $D^{MSS/sulfide}$ (Mungall et al., 2004) and known $D^{sulfide/silicate}$ (Mungall and Brenan, 2014)**.** As there was no data for Re and Os, the $D^{sulfide/silicate}$ is presented as well. It should be noted that both studied were done at ambient pressure and 1200 °C and 1050 °C for the $D^{sulfide/silicate}$, and $D^{MSS/sulfide}$ values respectively. When compared to the $D^{MSS/silicate}$ the partition coefficients for Cu, Rh, Re, and Pd show little variation, Pt shows 2 orders of magnitude higher than the MSS-silicate values. Ru, Os, and Ir vary from 2-1 orders of magnitude lower than the MSS-silicate values. This indicates that carbonate melts are better at transporting Ru and Ir and worse at transporting Pt compared to silicate melts. Regardless, the sulfide phase will still preferentially take up the precious metals.

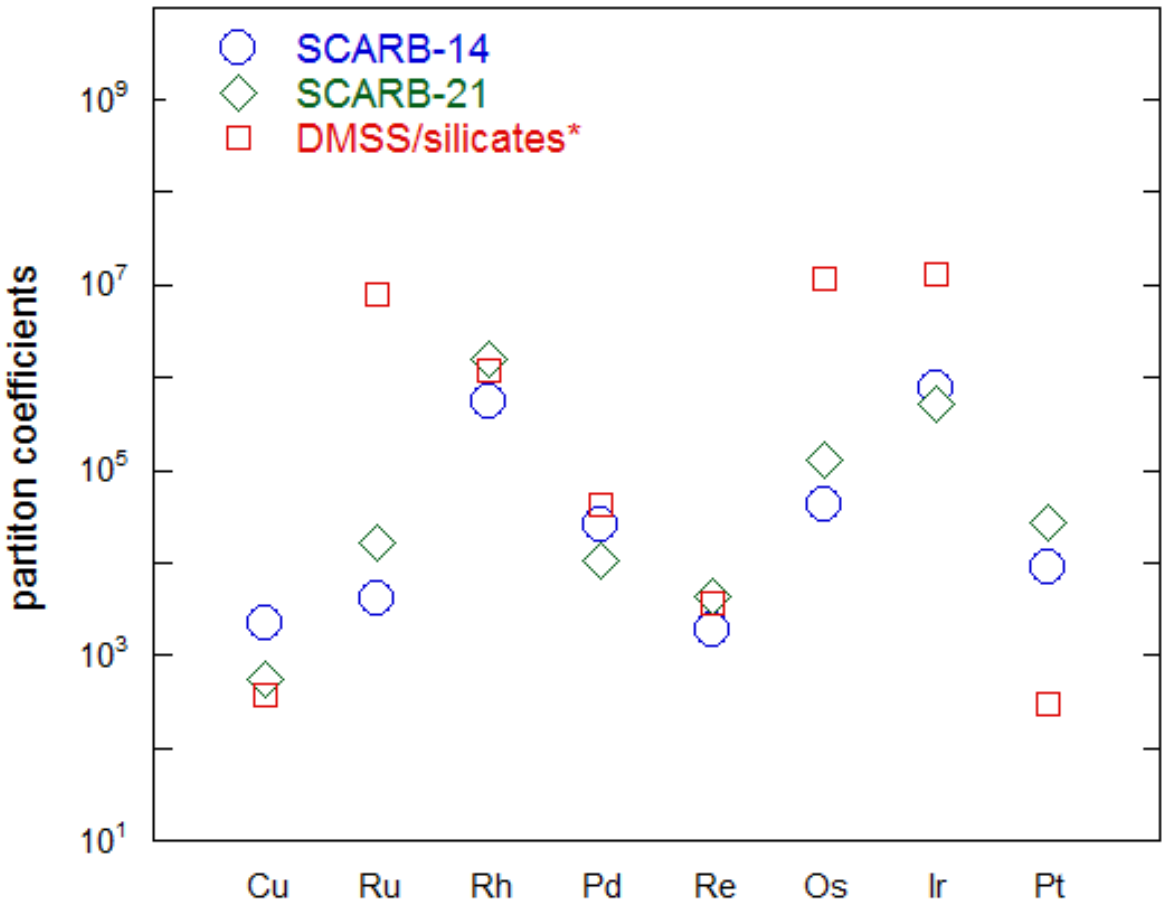

Figure 6.4 Partition coefficients for Cu, Re and PGEs. $D^{sulfide/carb}$ for SCARB-14 and SCARB-21. Both ran at 1200 ºC at 2Gpa. $D^{MSS/silicate}$ calculated from data from Mungall and Brenan (2014) and Liu and Brenan (2015).

The Os and Re partition coefficients have importance as they form a radiometric dating series based on the beta decay of ^{187}Re to ^{187}Os, which is often used as a dating method because of Re large half-life and the siderophilic/chalcophilic behavior (Shirey and Walker, 1998). One main assumptions with this is that there is no contamination from sulfides in the mantle. The partition coefficients from this study it indicates that there is a possibility of a carbonate melt transporting additional Os without Re, contaminating the system.

The question arises if the solubility of sulfur in carbonate melts can redistribute sulfur in the mantle? For this a mass balance is required:

$$C_{tot} = C_{sulf}X_{sulf} + C_{melt}X_{melt} \quad (15)$$

The concentration of sulfur in a depleted mantle is 200 ppm (Dasgupta and Hirchmann, 2006). Estimates of carbonate liquid in the mantle range from 0.03 to 0.3 % carbonate liquid produced at melting ridges, we'll use an estimate of 0.3 wt% for a maximum value (Dasgupta and Hirchmann, 2006). This 0.3 wt% carbonate liquid has an estimated average of 2000 ppm of sulfur, as determined in this study. Using equation 15 this gives a total of 0.0006 wt% of sulfur removed by carbonate melt, leaving 194 ppm of sulfur in the mantle. Clearly carbonate melts do not have the ability to significantly redistribute sulfur in the mantle.

Chapter 7: Summary and Conclusion

7.1 Sulfur and precious metals in carbonate melts

Experiments were performed at 1 and 2 GPa at both 1100 ºC and 1200 ºC. Run-products consist of a monosulfide solution or sulfide liquid coexisting with quenched carbonate melt, represented by a fine-grained intergrowth of carbonate phase and sulfide dendrites, which were analyzed to determine a melt reconstruction. Experiments completed up to Fe-saturation by adding up to 30 wt % Fe_2O_3 and the iron content in the carbonate remains quite low, ~4% FeO. The two primary finding in this study include 1) The solubility of sulfur in carbonate melts is higher than that of silicate melts at equivalent conditions by approximately an order of magnitude. Additionally, the sulfur solubility shows an exponential dependence on the FeO content of the melt and is invariant with temperature and time. 2) Precious metal partitioning of Cu and PGE was determined and shows to be similar or higher compared to silicate melts except for Ru and Ir, which shows $D^{sulf/carb}$ 1-2 orders of magnitude lower than that of the $D^{MSS/silicate}$. $D^{sulfide/silicate}$ values for Os are lower than the $D^{sulf/carb, Os}$ by an order of magnitude

7.2 Future work

Throughout the course of experimentation many strands of future work in regards to this question can be followed. First, there are several other compositions that could be done, no experiments with siliceous components or variations in the carbonate melts were studied. Carbonatites co-exist with peridotite assemblages (Wallace and Green, 1998) which indicates that there will be some siliceous component in a carbonate melt. Jugo et al. (2014) determined that the sulfur contents in sulfate-saturated melts is significantly higher than that of sulfide-saturated melts, which is another line of work to be further pursued. More experimentation with a pressure series is necessary to determine the relationship with the sulfur solubility with confidence. Additionally, more experiments to determine the partition coefficients of Cu, Au, and Re with varying f_{O2}-f_{S2} as sulfide-silicate partitioning has been shown to vary considerably.

References

Ammannati, E., Jacob, D.E., Avanzinelli, R., Foley, S.F. and Conticelli, S., 2016. Low Ni olivine in silica-undersaturated ultrapotassic igneous rocks as evidence for carbonate metasomatism in the mantle. Earth and Planetary Science Letters, 444:64-74.

Andrews, D.A., and Brenan, J.M. 2002. The solubility of ruthenium in sulfide liquid: implications for platinum group mineral stability and sulfide melt–silicate melt partitioning. Chem Geol 192:163−181

Barker, D.S. and Nixon, P.H., 1989. High-Ca, low-alkali carbonatite volcanism at Fort Portal, Uganda. Contributions to Mineralogy and Petrology. 103(2):166-177.

Brenan, J.M. 2008. Re–Os fractionation by sulfide melt–silicate melt partitioning: a new spin. Chemical Geology. 248(3):140-65.

Brenan, J.M., Bennett, N.R. and Zajacz, Z., 2016. Experimental results on fractionation of the highly siderophile elements (HSE) at variable pressures and temperatures during planetary and magmatic differentiation. Reviews in Mineralogy and Geochemistry, 81(1):1-87.

Brenan, J.M., and Li, C. 2000. Constraints on oxygen fugacity during sulfide segregation in the Voisey's Bay intrusion, Labrador, Canada. Economic Geology. 95(4):901-15.

Bockrath, C., Ballhaus, C., and Holzheid, A. 2004. Fractionation of the platinum-group elements during mantle melting. Science. 305(5692):1951-3.

Dasgupta R., Hirschmann M.M., 2006. Melting in the Earth's deep upper mantle caused by carbon dioxide. Nature. 440(7084):659-62.

Delpech, G., Lorand, J.P., Grégoire, M., Cottin, J.Y., and O'Reilly, S.Y. 2012. In-situ geochemistry of sulfides in highly metasomatized mantle xenoliths from Kerguelen, southern Indian Ocean. Lithos. 154:296-314

Fincham, C.J., and Richardson, F.D. 1954. The behaviour of sulphur in silicate and aluminate melts. In Proceedings of the Royal Society of London A: Mathematical, Physical and Engineering Sciences 223(1152):40-62

Freestone, I.C., and Hamilton, D.L. 1980. The role of liquid immiscibility in the genesis of carbonatites — An experimental study. Contrib Mineral Petrol 73(2):105-117

Fonseca, R.O.C., Campbell, I.H., O'Neill, H.St.C., and Allen, C.M. 2009. Solubility of Pt in sulphide mattes: Implications for the genesis of PGE-rich horizons in layered intrusions. Geochim Cosmochim Acta 73:5764−5777

Fontana, J. 2006. Phoscorite-Carbonatite Pipe Complexes. Platinum Metals Review, 50(3): 134-142

Fortin, M.A., Riddle, J., Desjardins-Langlais, Y. and Baker, D.R., 2015. The effect of water on the sulfur concentration at sulfide saturation (SCSS) in natural melts. Geochimica et Cosmochimica Acta, 160:100-116.

Gittins J (1989) The origin and evolution of carbonatite magmas. In: Carbonatites: Genesis and Evolution, Bell K (ed) Unwin Hyman, London, 580-600

Gittins J, Jago BC (1998) Differentiation of natrocarbonatite magma at Oldoinyo Lengai volcano, Tanzania. Mineral Mag 62:759-768

Giuliani, A., Kamenetsky, V.S., Phillips, D., Kendrick, M.A., Wyatt, B.A., and Goemann, K. 2012. Nature of alkali-carbonate fluids in the sub-continental lithospheric mantle. Geology. 40(11):967-70.

Hammouda, T., and Laporte, D. 2000. Ultrafast mantle impregnation by carbonatite melts. Geology. 28(3):283-5.

Helz, G.R. and Wyllie, P.J., 1979. Liquidus relationships in the system CaCO3- Ca (OH)2- CaS and the solubility of sulfur in carbonatite magmas. Geochimica et Cosmochimica Acta, 43(2): 259-265

Ionov, D.A., O'Reilly, S.Y., Genshaft, Y.S., and Kopylova, M.G. 1996. Carbonate-bearing mantle peridotite xenoliths from Spitsbergen: phase relationships, mineral compositions and trace-element residence. Contributions to Mineralogy and Petrology. 125(4):375-92.

Jones, A.P., Genge, M., and Carmody, L. 2013. Carbonate melts and carbonatites. Reviews in Mineralogy & Geochemistry. 75(1):289-322.

Jugo, P.J., Luth, R.W., and Richards, J.P. 2005. An experimental study of the sulfur content in basaltic melts saturated with immiscible sulfide or sulfate liquids at 1300° C and 1.0 GPa. Journal of Petrology. 46(4):783-98.

Kamenetsky, M.B., Sobolev, A.V., Kamenetsky, V.S., Maas, R., Danyushevsky, L.V., Thomas, R., Pokhilenko, N.P., and Sobolev, N.V. 2004. Kimberlite melts rich in alkali chlorides and carbonates: a potent metasomatic agent in the mantle. Geology. 32(10):845-8.

Kono, Y., Kenney-Benson, C., Hummer, D., Ohfuji, H., Park, C., Shen, G., Wang, Y., Kavner, A., and Manning, C.E. 2014. Ultralow viscosity of carbonate melts at high pressures. Nature communications. 5:1-8

Le Bas, M.J. 1987. Nephelinites and carbonatites. Geological Society, London, Special Publications. 30(1):53-83.

Liu, Y. and Brenan, J., 2015. Partitioning of platinum-group elements (PGE) and chalcogens (Se, Te, As, Sb, Bi) between monosulfide-solid solution (MSS), intermediate solid solution (ISS) and sulfide liquid at controlled fO 2–fS 2 conditions. Geochimica et Cosmochimica Acta, 159: 139-161.

Liu, Y., Samaha, N.T., Baker, D.R. 2007. Sulfur concentration at sulfide saturation (SCSS) in magmatic silicate melts. Geochimica et Cosmochimica Acta. 71(7):1783-99

Lorand, J.P., Delpech, G., Grégoire, M., Moine, B., O'Reilly, S.Y., and Cottin, J.Y. 2004. Platinum-group elements and the multistage metasomatic history of Kerguelen lithospheric mantle (South Indian Ocean). Chemical Geology. 208(1):195-215.

Martin, L.H., Schmidt, M.W., Mattsson, H.B., and Guenther, D. 2013. Element partitioning between immiscible carbonatite and silicate melts for dry and H2O-bearing systems at 1–3 GPa. Journal of Petrology. 54(11): 2301 - 2338

Mavrogenes, J.A., and O'Neill H.S.C. 1999. The relative effects of pressure, temperature and oxygen fugacity on the solubility of sulfide in mafic magmas. Geochimica et Cosmochimica Acta. 63(7):1173-80

Minarik, W.G., and Watson, E.B. 1995. Interconnectivity of carbonate melt at low melt fraction. Earth and Planetary Science Letters. 133(3-4):423-37.

Mungall, J.E., Andrews, D.R., Cabri, L.J., Sylvester, P.J., and Tubrett, M. 2005. Partitioning of Cu, Ni, Au, and platinum-group elements between monosulfide solid solution and sulfide melt under controlled oxygen and sulfur fugacities. Geochimica et Cosmochimica Acta. 69(17):4349-60.

Mungall, J.E., and Brenan, J.M. 2014. Partitioning of platinum-group elements and Au between sulfide liquid and basalt and the origins of mantle-crust fractionation of the chalcophile elements. Geochimica et Cosmochimica Acta. 125:265-89.

Nelson, D.R., Chivas, A.R., Chappell, B.W., and McCulloch, M.T. 1988 Geochemical and isotopic systematics in carbonatites and implications for the evolution of ocean-island sources. Geochimica et Cosmochimica Acta. 52(1):1-7.

O'Neill, H.S.C. and Mavrogenes, J.A., 2002. The sulfide capacity and the sulfur content at sulfide saturation of silicate melts at 1400 C and 1 bar. Journal of Petrology, 43(6):1049-1087

Olafsson, M. and Eggler, D.H. 1983. Phase relations of amphibole, amphibole-carbonate, and phlogopite-carbonate peridotite: petrologic constraints on the asthenosphere. Earth and Planetary Science Letters. 64(2):305-15.

Rao, N.C., Anand, M., Dongre, A., and Osborne, I. 2010. Carbonate xenoliths hosted by the Mesoproterozoic Siddanpalli Kimberlite Cluster (Eastern Dharwar craton): implications for the geodynamic evolution of southern India and its diamond and uranium metallogenesis. International Journal of Earth Sciences. 99(8):1791-804.

Ripley, E.M., and Li, C. 2013. Sulfide Saturation in Mafic Magmas: Is External Sulfur Required for Magmatic Ni-Cu-(PGE) Ore Genesis?. Economic Geology.108(1):45-58.

Rudashevsky, N.S., Kretser, Y.U.L., Bulakh, A.G., and Rudashevsky, V.N. 2001. Two types of PGE mineralisations in carbonatite deposits (Phalaborwa Massif, South Africa and Kovdor Massif, Russia). Journal of African Earth Sciences, 32(1):A30

Shirey, S.B., and Walker, R.J. 1998. The Re-Os isotope system in cosmochemistry and high-temperature geochemistry. Annual Review of Earth and Planetary Sciences. (1):423-500.

Wallace, M.E. and Green, D.H. 1988. An experimental determination of primary carbonatite magma composition. Nature 335: 343-346

Widom, E., Kepezhinskas, P., and Defant, M. 2003. The nature of metasomatism in the sub-arc mantle wedge: evidence from Re–Os isotopes in Kamchatka peridotite xenoliths. Chemical Geology.196(1):283-306.

Woolley, A.R. and Bailey, D.K. 2012.The crucial role of lithospheric structure in the generation and release of carbonatites: geological evidence. Mineralogical Magazine. 76(2):259-70.

Ulmer, P., and Luth, R.W. 1991. The graphite-COH fluid equilibrium in P, T, fO2 space. Contributions to Mineralogy and Petrology. 106(3):265-72.

Appendix A – Error Analysis and Melt reconstruction

Standard deviations are used for the errors of most averages. Because different associated errors, error propagation is required for the mass fractionation calculation. Recall the sulfur total is an addition of the S in the matrix and the dendrites, so these this errors are additional. The contribution of sulfur to the total melt content from the dendrites is from this equation:

$$S_{TOTden} = \frac{\sqrt{A^3_{sulfide}}\rho_{sulfide}}{\sqrt{A^3_{sulfide}}\rho_{sulfide}+\sqrt{A^3_{carb}}\rho_{carb}} \times S_{den} \quad \text{(A1)}$$

The errors from the S in the dendrites involves more error propagation which is done by evaluating each part of equation Al. The error for $A^{3/2}*\rho$ in the numerator is given by

$$\frac{\partial N}{|N|} = \frac{3}{2}\frac{\delta As}{|As|} \quad \text{(A2)}$$

Where *N* is the product of $A^{3/2}*\rho$ and As is the area of the respective sulfides, determined by Image J analysis. For the denominator, the absolute error for each term is required:

$$\delta D1 = \left|\frac{3}{2}\right| \sqrt{As}\delta As \quad \text{(A3)}$$

Where D1 is the product of the first term of the denominator, the second term is the same as the carbonate melt area. The error from each component of the denominator is propagated to yield this equation:

$$\delta D = \sqrt{\left(\left|\frac{3}{2}\right| \sqrt{As}\delta As\right)^2 + \left(\left|\frac{3}{2}\right| \sqrt{Ac}\delta Ac\right)^2} \quad \text{(A4)}$$

Where δD is the error of the denominator. The total error for the mass fraction (MF) calculation in A1 is as follows:

$$\frac{\delta MF}{|MF|} = \sqrt{\left(\frac{\delta N}{N}\right)^2 + \left(\frac{\delta D}{D}\right)^2} = \sqrt{\left(\frac{3}{2}\frac{\delta As}{|As|}\right)^2 + \left(\frac{\sqrt{\left(\left|\frac{3}{2}\right|\sqrt{As}\delta As\right)^2 + \left(\left|\frac{3}{2}\right|\sqrt{Ac}\delta Ac\right)^2}}{\sqrt{A_s^3}\rho_s + \sqrt{A_c^3}\rho_c}\right)^2} \quad \text{(A5)}$$

The mass fraction is then multiplied by S_{den} which is the S content of the dendrites. Error for the sulfur total from the dendrites (S_{TD}) then becomes:

$$\delta s_{TD} = |s_{TD}|\sqrt{\left(\frac{\delta MF}{MF}\right)^2 + \left(\frac{\partial s_{den.}}{s_{den}}\right)^2} =$$

$$|s_{TD}|\sqrt{\left(\sqrt{\left(\frac{3}{2}\frac{\delta As}{|As|}\right)^2 + \left(\frac{\sqrt{\left(\left|\frac{3}{2}\right|\sqrt{As}\delta As\right)^2 + \left(\left|\frac{3}{2}\right|\sqrt{Ac}\delta Ac\right)^2}}{\sqrt{A_s^3}\rho_s + \sqrt{A_c^3}\rho_c}\right)^2}\right)^2 + \left(\frac{\partial s_{den.}}{s_{den}}\right)^2} \quad \text{(A6)}$$

Note the error from the S_{den} content is just error associated with the average and not the analytical error of the microprobe (which is relatively negligible). The S_{TD} value is then added to the sulfur from the matrix as per equation A7:

$$\sum S_{Total} = S_{matrix} + S_{TOTden} \quad \text{(A7)}$$

$$\delta S_{\dot{T}} = \sqrt{(\delta s_{mat})^2 + \left(|s_{TD}|\sqrt{\left(\sqrt{\left(\frac{3}{2}\frac{\delta As}{|As|}\right)^2 + \left(\frac{\sqrt{\left(\left|\frac{3}{2}\right|\sqrt{As}\delta As\right)^2 + \left(\left|\frac{3}{2}\right|\sqrt{Ac}\delta Ac\right)^2}}{\sqrt{A_s^3}\rho_s + \sqrt{A_c^3}\rho_c}\right)^2}\right)^2 + \left(\frac{\partial s_{den.}}{s_{den}}\right)^2}\right)^2} \quad \text{(A8)}$$

Where the error from the sulfur in the matrix (S_{mat}) is just the standard deviation and the instrument error (counting statistics) is assumed negligible. Table A1 shows calculations of the error and the S_{tot} melt reconstruction.

Table A1 Melt reconstruction and error analysis.

	As avg	As σ	Ac avg	Ac σ	N*	D*	MF	δN/N	δD	δD/D	δMF/MF	Dendrites (wt%) S avg	Dendrites (wt%) S σ	Stot den	δStot den	WDS (wt%) S_m**	WDS (wt%) $\delta S_m/S_m$	WDS (wt%) δS_m	ppm S TOT	ppm δS TOT
SCARB-1	0.72	0.20	99.28	0.20	2.79	2139.65	1.31E-03	0.42	2.98	1.39E-03	0.42	28.10	1.91	0.04	0.02	0.05	14.82	0.01	845.51	170.08
SCARB-4	0.32	0.14	99.68	0.14	0.82	2150.41	3.81E-04	0.68	2.14	9.96E-04	0.68	37.75	0.50	0.01	0.01	0.11	7.32	0.01	1256.41	127.11
SCARB-5	1.75	0.72	98.25	0.72	10.73	2114.13	5.07E-03	0.61	10.79	5.10E-03	0.61	30.91	0.69	0.16	0.10	0.00	0.00	0.00	1568.26	964.78
SCARB-6	1.37	0.63	98.63	0.63	7.43	2123.07	3.50E-03	0.68	9.38	4.42E-03	0.68	35.86	0.58	0.13	0.09	0.01	47.61	0.01	1369.70	859.46
SCARB-8	4.54	1.12	95.39	1.12	44.62	2057.11	2.17E-02	0.37	16.76	8.15E-03	0.37	25.12	2.14	0.54	0.21	0.00	0.00	0.00	5448.38	2066.47
SCARB-10	4.09	1.40	96.02	1.40	38.14	2070.34	1.84E-02	0.51	20.96	1.01E-02	0.51	20.48	2.76	0.38	0.20	0.01	46.56	0.01	3892.29	2000.35
SCARB-11	2.94	1.24	97.06	1.24	23.24	2088.75	1.11E-02	0.63	18.56	8.88E-03	0.63	29.03	1.66	0.32	0.20	0.00	0.00	0.00	3229.90	2048.41
SCARB-14	0.26	0.11	99.74	0.11	0.61	2152.18	2.85E-04	0.62	1.62	7.53E-04	0.62	37.62	0.83	0.01	0.01	0.00	0.00	0.00	107.33	66.82
SCARB-15	1.21	0.34	98.79	0.34	6.17	2126.96	2.90E-03	0.42	5.16	2.43E-03	0.42	33.46	3.47	0.10	0.04	0.14	6.27	0.01	2364.22	433.60
SCARB-16	1.07	0.43	98.93	0.43	5.11	2130.53	2.40E-03	0.61	6.52	3.06E-03	0.61	18.12	2.61	0.04	0.03	0.01	46.31	0.01	568.44	279.03
SCARB-21	1.12	0.45	98.88	0.45	5.44	2129.39	2.55E-03	0.60	6.69	3.14E-03	0.60	22.39	2.51	0.06	0.03	0.09	8.57	0.01	1502.98	357.95

* From equation A1, ρ_s = 4.62 g/cm^3 pyrrhotite analogue (Mindat.com) from ρ_c = 2.16 g/cm^3 (Jones et al. 2013)
**0 values are because the lowest S was below the minimum detection limit, so assumed to be zero.
As is the area of the sulfides, Ac is the area of the carbonate melt, avg is the average and σ is the standard deviation.

Table A2. Sulfide dendrite compositions determined by EDS

wt %	Fe	S
SCARB-1	50.23	28.10
err	4.91	3.85
SCARB-4	57.60	37.75
err	0.55	0.50
SCARB-5	62.85	30.91
err	1.03	0.69
SCARB-6	62.00	35.86
err	1.02	0.58
SCARB-8	73.40	25.12
err	2.34	2.14
SCARB-10	71.62	20.48
err	1.13	2.76
SCARB-11	67.62	29.03
err	1.92	1.66
SCARB-14	49.45	37.62
err	1.19	0.83
SCARB-15	56.56	33.46
err	3.64	3.47
SCARB-16	45.31	18.12
err	4.23	2.61
SCARB-21	41.16	22.39
err	3.00	2.51
avg	57.98	28.98

Appendix B – Partition Coefficient Calculations

Table B1. Calculations of Cu partition coefficients

	Sulfide	Carbonate	Sulfide/Carb = $D^{sulf/carb, Cu}$
SCARB-4	4662.65	15.82	294.73
SCARB-5	5637.82	3.46	1630.61
SCARB-6	4869.87	2.04	2384.27
SCARB-8	4564.52	4.52	1009.29
SCARB-10	4976.70	3.85	1292.65
SCARB-11	3398.13	3.33	1021.23
SCARB-14*	9225.55	4.13	2233.79
SCARB-15*	9293.47	46.19	201.20
SCARB-16	4198.88	5.00	839.78
SCARB-21*	6490.89	11.55	561.98

* Sulfide analysis are from microprobe except for SCARB-14,-15, and -21

Table B1 shows the calculations for the Cu partition coefficients. $D^{sulf/carb, Cu}$ is equal to the Cu in the sulfide, measured with the microprobe, aside from SCARB-14,-15, and -21 as noted, divided by the Cu in the carbonate melt.

Table B2 Calculations of PGE partition coefficients

	Ni	Cu	Ru	Rh	Pd	Re	Os	Ir	Pt
SCARB-14 sulfide	13021	9226	201	2406	3448	253	410	385	2049
SCARB-14 carb melt	6.84	4.13	0.05	0.00	0.13	0.13	0.01	0.00	0.23
$D^{sulf/carb}$	**1903**	**2234**	**4109**	**534611**	**26322**	**1884**	**42272**	**755137**	**9029**
SCARB-15 sulfide	10640	9293	0.43	0.38	0.44	0.30	0.01	1	54
SCARB-15 carb melt	29.46	46.22	0.04	0.00	0.06	0.01	0.01	0.00	0.87
$D^{sulf/carb}$	**361**	**201**	**11**	**182**	**7**	**24**	**1**	**226**	**61**
SCARB-21 sulfide	12188	6491	484	3534	3795	410	1030	1320	2593
SCARB-21 carb melt	4.78	11.55	0.03	0.00	0.36	0.10	0.01	0.00	0.10
$D^{sulf/carb}$	**2550**	**562**	**16117**	**1606394**	**10661**	**4306**	**128744**	**527941**	**26456**

Table B2 shows the calculations for the PGE partition coefficients. The average PGE content in the sulfide is divided by the minimum carbonate melt composition value $D^{sulf/carb, PGE}$. All data is measured with LA-ICP-MS.